



Regulating the double-site Mn₂-N₆ electronic structure by manganese clusters for enhanced oxygen reduction

Guangtao Luo^{a,b,1}, Enze Zhu^{a,b,1}, Chaoyang Shi^{a,b}, Yanrong Ren^{a,b}, Yan Lin^a, Xikun Yang^c, Mingli Xu^{a,b,*}

^a Faculty of Metallurgical and Energy Engineering, Kunming University of Science and Technology, Kunming 650093, China

^b National and Local Joint Engineering Research Center of Lithium-ion Batteries and Materials Preparation Technology, Kunming 650093, China

^c Research Center for Analysis and Measurement, Kunming University of Science and Technology, Kunming 650093, China

ARTICLE INFO

Keywords:

Homonuclear double-site
Single-atom catalyst
Mn clusters
Axial traction effect
Oxygen reduction reaction

ABSTRACT

Effectively designing the coordination environment of metal atoms in single-atom catalysts to enhance the oxygen reduction reaction (ORR) performance is challenging. Herein, a strategy for regulating the electronic structure of double-site Mn₂-N₆ by axial traction of Mn cluster is presented. The atomically dispersed homonuclear double-site Mn₂-N₆ was synthesized. Experimental investigations and theoretical calculations revealed that the oxygen adsorption capacity of double-site Mn₂-N₆ was stronger than that of Mn-N₄, which can improve the weak adsorption of oxygen at isolated Mn active sites. The introduction of Mn clusters broke the planar structure of Mn₂-N₆ through axial traction, further altering the electron configuration around the active sites and effectively decreasing the adsorption strength of oxygen-containing intermediates and reaction energy barriers, leading to increased intrinsic activity, which greatly improved the ORR performance ($E_{1/2} = 0.91$ V). This work presented a novel way of regulating the electronic structure of homonuclear double single-atom sites by clusters.

1. Introduction

In recent years, single-atom catalysts (SACs) loaded with nitrogen-doped carbon (NC) materials have shown excellent electrocatalytic performance in improving the oxygen reduction reaction (ORR) on the cathode side of fuel cells and metal-air batteries [1–6]; these materials are expected to solve the problems of scarce resources, high cost and inadequate stability of current commercial Pt-based catalysts [7–9]. However, an isolated active site of SACs determines a fixed adsorption pattern, whereas the adsorption energies of intermediates of a multi-step reaction connected to an individual metal site are interrelated [10–15]. Optimally regulating the adsorption and desorption of each reaction intermediate at an individual active site simultaneously for a given multi-step reaction is extremely difficult [16–19]. This phenomenon is known as the scale relationship limit (SRL) and greatly hinders the development of pure SACs [20,21]. To solve this problem, researchers have developed dual single-atom catalysts (DACs), which can provide additional adsorption sites to form bonds with the two ends of adsorbates to further increase the bonding strength between the target

intermediates and the active sites. Moreover, electronic transfer can occur between heteronuclear atoms of dual single-atom catalysts [22–28]. For example, Cai et al. developed a FeMn/N-C bimetallic catalyst in which the introduction of Mn increased the density of FeN₄ active sites and modulated the electronic structure of FeN₄ sites to retain more FeN₄ sites embedded in the carbon matrix through the formation of FeN₄-O-MnN₄ structures. Density functional theory (DFT) calculations showed that the total energy barrier of the ORR decreased for the FeN₄-O-MnN₄ moiety, which greatly enhanced the ORR performance [29]. However, such conventional Fe-Mn-based heteronuclear dual single-atom catalysts need to rely on electron transfer between Mn and Fe to optimize the adsorption and desorption of oxygen-containing intermediates at Fe active sites, and the only real active site is Fe, which has a low atom utilization rate. In contrast, the advantage of homonuclear such as Mn-Mn dual single-atom is that no electron transfer is involved between the Mn atoms, both Mn are active sites, and the more active sites, the better the ORR performance. Several researchers have also investigated cluster-based single-atom catalysts in recent years and found that the introduction of clusters can cause electronic

* Corresponding author: Faculty of Metallurgical and Energy Engineering, Kunming University of Science and Technology, Kunming 650093, China.

E-mail address: xumingli0326@126.com (M. Xu).

¹ These authors contributed equally.

reconfiguration at the active sites of metal, which in turn can change the adsorption strength of adsorbates [30–33]. For example, Wang et al. reported a catalyst with iron clusters to modify individual FeN₄ sites. The introduction of iron clusters changed the electronic structure of FeN₄ in the active site, which changed the d-band centers of Fe in FeN₄ and decreased the adsorption of oxygen-containing intermediate OH* to accelerate the ORR, so that these changes together considerably enhanced the ORR performance [34].

Moreover, manganese with a 3d⁵4s² outer electronic structure provides favorable conditions for the controllable preparation of electrocatalysts with high ORR performance, primarily because Mn is abundant and inexpensive, and has high reactivity and a controllable coordination structure [35–38]. Additionally, Mn-based catalysts are almost free of Fenton reactions, which can make them more favorable for four-electron reactions [15]. Compared to Fe-based single-atom catalysts, Mn-based single-atom catalysts exhibit weaker adsorption of oxygen-containing intermediates, which is favorable for the desorption step of OH*, thereby accelerating the ORR process [22]. However, the oxygen adsorption capacity of conventional Mn-based single-atom catalysts is insufficient [24], and the oxygen adsorption capacity is considerably inferior to that of Fe-based single-atom catalysts. Thus, most ORR single-atom catalysts are designed with Fe as the active center. However, few studies have investigated the problem of insufficient oxygen adsorption capacity of Mn-based single-atom catalysts. Recently developed dual single-atom catalysts can greatly improve the adsorption capacity for oxygen due to their two neighboring active sites, which might solve the problem of difficulty in the adsorption of oxygen by Mn-based single-atom catalysts [21]. Introducing Mn clusters can reconfigure the electronic structure at the active sites of Mn, which can further regulate the adsorption strength of oxygen-containing intermediates at the active sites and, thus, achieve enhanced ORR performance.

In this work, we propose a new strategy to regulate the electronic structure of Mn active sites by using manganese chloride as the Mn precursor and glycine as the chelating ligand to coordinate Mn²⁺ before high-temperature carbonization. In this strategy, the agglomeration of a large quantity of Mn can be effectively avoided in the subsequent carbonization process. Additionally, catalysts with homonuclear double-site Mn₂-N₆ and Mn clusters were controllably synthesized by effectively introducing Mn clusters in a secondary carbonization step; inevitably, isolated Mn single-atom sites may also exist in these catalysts. The obtained catalyst had a high specific surface area (1524 m² g⁻¹) and a large number of active sites, and exhibited excellent ORR performance in an alkaline medium (0.1 M KOH: E_{1/2} = 0.91 V (vs. RHE)), which was significantly greater than that of the commercial Pt/C catalyst (E_{1/2} = 0.86 V). DFT calculations showed that the unique bridge adsorption pattern of Mn homonuclear double single-atoms facilitated the adsorption of oxygen during the ORR process, which solved the problem related to the low adsorption capacity of isolated Mn active sites for the adsorption of oxygen. Furthermore, the introduction of Mn clusters can disrupt the planar structure of the Mn₂-N₆ through axial traction, which can lead to electronic reconfiguration of Mn₂-N₆ sites, lowering of the d-band center of Mn, and weakening of the adsorption of the oxygen-containing intermediate OH* on the catalyst [31]. These changes improved the ORR performance. This strategy of modifying homonuclear double single-atom sites with metal clusters provides a new insight into the optimization of electronic structures to boost electrocatalytic performance in the future.

2. Experimental section

2.1. Chemicals

Manganese chloride tetrahydrate (MnCl₂·4H₂O), glycine (NH₂CH₂COOH) and hydrochloric acid (HCl) were all purchased from Macklin (Shanghai China). Commercial Pt/C catalyst (Johnson Matthey, 20 wt%) were purchased from Hesen (Shanghai China).

2.2. Synthesis of catalysts

2.2.1. Synthesis of Glycine-MnCl₂ precursor

The MnCl₂·4H₂O (1.972 g), water (50 mL), alcohol (40 mL) and glycine (1.5 g) were added to a 100 mL beaker, sonicated for 2 hours, then dried in an oil bath at 60 °C to obtain a white solid, and the white solid was ground into powder to obtain glycine-MnCl₂.

2.2.2. Synthesis of Mn_{cluster}/Mn_{DAC}-N-C

The as-prepared Glycine-MnCl₂ precursor were carbonized in flowing N₂ in a tube furnace using a heating rate of 5 °C min⁻¹ up to 900 °C, dwell for 2 h to obtain MnO/Mn-N-C catalyst with MnO particles. Next, the MnO/Mn-N-C were added to 40 mL 1 mol L⁻¹ of HCl and stirred for 6 h at room temperature, filtered and cleaned, and placed in a drying oven at 60 °C to dry overnight to obtain Mn_{DAC}-N-C catalyst. Finally, the Mn_{DAC}-N-C were carbonized in flowing N₂ in a tube furnace using a heating rate of 5 °C min⁻¹ up to 900 °C, dwell for 2 h to obtain the final catalyst Mn_{cluster}/Mn_{DAC}-N-C.

2.2.3. Synthesis of Mn_{cluster}/Mn_{SAC}-N-C

The Mn_{cluster}/Mn_{SAC}-N-C catalyst was prepared under the similar conditions as the synthesis of Mn_{cluster}/Mn_{DAC}-N-C mentioned above, except that the addition amount of MnCl₂·4H₂O was less than that for Mn_{cluster}/Mn_{DAC}-N-C, which is 0.986 g.

2.2.4. Synthesis of Mn_{SAC}-N-C

The Mn_{SAC}-N-C catalyst was prepared under the similar conditions as the synthesis of Mn_{DAC}-N-C mentioned above, except that the addition amount of MnCl₂·4H₂O was less than that for Mn_{DAC}-N-C, which is 0.986 g.

2.2.5. Synthesis of N-C

The N-C catalyst was prepared under the similar conditions as the synthesis of Mn_{cluster}/Mn_{DAC}-N-C mentioned above, except that no Mn source was added in glycine-MnCl₂ precursor.

2.3. Material characterization

The Powder X-ray diffraction (XRD) patterns were recorded using an Empyrean diffractometer with Cu Kα radiation at a scanning rate of 5 °C min⁻¹. The absorption-desorption isotherms of nitrogen and pore size distribution were determined using a Brunauer-Emmett-Teller (BET) surface area operator (Quantachrome EVO). The physical morphology of the samples was characterized via field emission scanning electron microscopy (FEI Nova NanoSEM 450), TEM, and high-resolution TEM (JEOL JEM-F200). High-angle annular dark-field scanning transmission electron microscopy (HAADF-STEM) images were recorded using a JEOL JEM-ARM200F Atomic Resolution Analytical Electron Microscope with a spherical aberration corrector working at 300 kV. X-ray photoelectron spectroscopy (XPS) was conducted using Al Kα radiation (PHI 5000 Versaprobe III). The content of Mn in all the samples was analyzed via ICP—OES (Agilent 5110 (OES)). Raman spectroscopy analysis was performed using a WITec alpha300R Raman microscope. The X-ray absorption fine structure spectra (XAFS) were recorded at SPRING-8 in fluorescence mode. The storage rings of the BSRF were operated at 2.5 GeV with a maximum current of 250 mA. Using a Si (111) double-crystal monochromator, the data were collected in transmission mode using an ionization chamber. All the spectra were collected under ambient conditions.

2.4. Electrochemical measurements using RDE and RRDE

All the electrochemical performance measurements were conducted using a three-electrode system and an electrochemical workstation (CHI 760E). A glassy carbon rotating disk electrode (RDE, diameter 5 mm) or a ring-rotated disk electrode (RRDE, diameter 6 mm) covered with

catalyst film (loading 0.6 mg cm⁻² for samples and 0.2 mg cm⁻² for commercial Pt/C) was used as the working electrode substrate. A Pt foil was used as the counter electrode and an Ag/AgCl (saturated KCl) electrode was used as the reference electrode.

Cyclic voltammetry (CV) and linear sweep voltammetry (LSV) curves were obtained in N₂/O₂-saturated 0.1 M KOH or 0.1 M HClO₄ electrolyte solutions at scan rates of 50 mV s⁻¹ and 5 mV s⁻¹, respectively.

The measured potential vs. Ag/AgCl was converted to the reversible hydrogen electrode (RHE) scale, according to the following equation:

$$E(\text{RHE}) = E(\text{Ag/AgCl}) + 0.0591 \times \text{pH} + 0.197 \text{ V} \quad (1)$$

The kinetic current density was calculated according to the Koutecky Levich equation:

$$\frac{1}{J} = \frac{1}{J_k} + \frac{1}{J_L} \quad (2)$$

Here, J represents the current density normalized by the geometric area (mA cm⁻²); J_k and J_L represent the kinetic current density and the limiting diffusion current density, respectively.

The electron transfer number (n) and hydrogen peroxide yield (H₂O₂ %) were determined by the RRDE and calculated using the following equations:

$$n = 4 \times \frac{I_D}{\frac{I_R}{N} + I_D} \quad (3)$$

$$\text{H}_2\text{O}_2(\%) = 200 \times \frac{\frac{I_R}{N}}{\frac{I_R}{N} + I_D} \quad (4)$$

Here, I_D represents the disk current, I_R represents the ring current, and N ($N = 0.37$) represents the Pt ring collection efficiency.

The electrochemically active surface area (ECSA) was determined by the non-faradic double-layer capacitance and obtained by the following equation:

$$\text{ECSA} = \frac{C_{dl}}{C_s} \quad (5)$$

where C_{dl} is the double layer capacitance, C_s is the specific capacitance, and the midpoint common capacitance of 40 μF cm⁻² is taken as its value.

The turnover frequency (TOF) was calculated by normalizing the kinetic current density based on the following equation:

$$\text{TOF} = \frac{J_k N_e M_{\text{Mn}}}{C_{\text{cat}} N_A W_{\text{Mn}}} \quad (6)$$

N_e represents the number of electrons per coulomb (6.24×10^{18} e C⁻¹). M_{Mn} represents the molar mass of Mn (54.938 g mol⁻¹). N_A represents the Avogadro constant (6.022×10^{23} mol⁻¹). C_{cat} represents the catalyst loading (0.6 mg cm⁻²). W_{Mn} represents the weight percentage of Mn measured via ICP-OES.

The OER activities of the catalysts were measured by a conventional three electrode at a scan rate of 5 mV s⁻¹ in O₂-saturated 1.0 M KOH, where Pt foil was employed as the counter electrode. The iR compensation was performed by electrochemical impedance spectroscopy to correct the compensated potential. Electrochemical impedance spectroscopy (EIS) measurements were evaluated over the frequency range from 100 kHz to 0.01 Hz.

2.5. Zn-air battery test

The zinc-air cell was tested using a mixture of 6.0 M KOH and 0.2 M ZnAc₂ as the electrolyte. A Zn sheet (0.2 mm thick) was used as the negative electrode, and the surface oxide layer was removed by sandpaper before use. The air-side electrode base material was prepared by rolling hydrophobic carbon paper, waterproof and breathable

membranes (made of PFTE and carbon powder), and foam nickel catalyst together. After coating the carbon paper with the catalyst, the composite electrode material was obtained as the air cathode, in which the load of Mn_{cluster}/Mn_{DAC}-N-C was 1.0 mg cm⁻² and the load of commercial Pt/C was 1.0 mg cm⁻². The formula for calculating the power density was as follows:

$$\text{Power density} = \text{Current density} \times \text{Voltage} \quad (7)$$

The discharge-specific capacity of the battery was calculated using the following formula after constant current discharge at 10 mA cm⁻²:

$$\text{Specific capacity} = \frac{\text{Current} \times \text{servicehours}}{\text{weight of consumed Zine}} \quad (8)$$

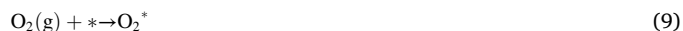
2.6. Computational methods

The first principles were used to perform all spin-polarization density functional theory (DFT) calculations within the generalized gradient approximation (GGA) using the Perdew-Burke-Ernzerhof (PBE) formulation in the CASTEP code. The geometry optimizations were performed using the Broyden-Fletcher-Goldfarb-Shanno (BFGS) algorithm. The kinetic cut-off energy of the plane-wave basis was 450 eV. The convergence criteria for the total energy and forces were set as 10⁻⁵ eV and 0.01 eV Å⁻¹, respectively. The vacuum spacing in the direction perpendicular to the plane of the structure was 12 Å. Brillouin zone integration was performed by 2 × 2 × 1 Monkhorst-Pack k-point sampling for the structure.

The formation energies of Mn_{SAC}-N-C, Mn_{DAC}-N-C, Mn_{cluster}/Mn_{SAC}-N-C, and Mn_{cluster}/Mn_{DAC}-N-C were embedded into the graphene matrix. The formation energy was calculated as $F = E_{\text{tot}} - nC_{\text{ev}} - nN_{\text{ev}} - nMn_{\text{ev}}$, where F indicates the formation energy, E_{tot} indicates the total energy, and n indicates the number of atoms. C_{ev} , N_{ev} , and Mn_{ev} indicate the energy per atom in graphene, N₂ gas molecule, and Mn cluster, respectively (the number of Mn atoms in the cluster was 7).

2.6.1. DFT calculations of the reaction mechanism

The ORR associated with the catalysts involved a two-electron pathway or a four-electron pathway. In an alkaline medium (pH = 14), H₂O acts as a proton donor. The four-electron pathway might proceed through two possible mechanisms: the associative pathway, which involves the protonation of O₂, or the direct O₂ dissociation pathway. Here, the associative pathway was used because it often dominates the dissociative mechanism when the applied bias potential is low. In an alkaline electrolyte, the four-electron ORR occurred as follows:



Here, $*$ represents an active site on the catalytic surface, and O*, OH*, and OOH* are adsorbed intermediates [39].

2.6.2. DFT calculation of reaction free energy

The Gibbs reaction free energy of these elementary steps was obtained via DFT calculations based on the computational normal hydrogen electrode (NHE) model. The NHE was set as the reference electrode. The free energy of the adsorption of O*, OH*, and OOH* was used to calculate the reaction free energy of each elementary step in the ORR. The exact free energies of OOH, O, and OH radicals in the electrolyte solution were difficult to obtain, and were determined relative to

the free energies of stoichiometrically appropriate amounts of H_2O (l) and H_2 (g). For each elementary step, Gibbs free energy difference was calculated using the following equation:

$$\Delta G = \Delta E + \Delta \text{ZPE} - T\Delta S + \Delta G_U + \Delta G_{\text{PH}} \quad (14)$$

Here, ΔE and ΔZPE represent the total energy change obtained from DFT calculations and the change in zero-point energy (ZPE), respectively; T and ΔS represent the temperature (298 K) and the change in entropy, respectively; ΔG_U represents the contribution of the applied potential, $\Delta G_U = -eU$, e and U represent the transferred charge and the applied potential; and ΔG_{PH} represents the correction of the H^+ free energy, which is conducted based on the following equation[24,25,34]:

$$\Delta G_{\text{PH}} = -k_B T \ln[\text{H}]^+ = k_B T \ln 10 \times \text{pH} \quad (15)$$

Here, k_B represents the Boltzmann constant.

The free energy of O_2 molecules was calculated as follows: $G_{\text{O}_2} = 2G_{\text{H}_2\text{O}} - 2G_{\text{H}_2} + 4.92$. The free energy of OH^- was calculated as follows: $G_{\text{OH}^-} = G_{\text{H}_2\text{O}} - G_{\text{H}^+}$, where $G_{\text{H}^+} = 1/2G_{\text{H}_2} - k_B T \ln 10 \times \text{pH}$. The free energy of adsorption of the reaction intermediates was calculated as follows:

$$\Delta G_{\text{O}_2^*} = G_{\text{O}_2^*} - G_* + 2G_{\text{H}_2} - 4.92 \quad (16)$$

$$\Delta G_{\text{OOH}^*} = G_{\text{OOH}^*} - G_* + 1.5G_{\text{H}_2} - 2G_{\text{H}_2\text{O}} \quad (17)$$

$$\Delta G_{\text{O}_2^*} = G_{\text{O}_2^*} - G_* + 0.5G_{\text{H}_2} - G_{\text{H}_2\text{O}} \quad (18)$$

$$\Delta G_{\text{OH}^*} = G_{\text{OH}^*} - G_* + 0.5G_{\text{H}_2} - G_{\text{H}_2\text{O}} \quad (19)$$

3. Results and discussion

3.1. Theoretical prediction of Mn clusters regulating double-site $\text{Mn}_2\text{-N}_6$ for oxygen reduction reaction

In order to investigate the effects of the introduction of Mn clusters on the coordination environment, geometry, and electronic structure of Mn in MnN_4 single-atom sites and $\text{Mn}_2\text{-N}_6$ dual-single-atom sites, as well as the changes in ORR properties resulting from these effects, four structural models, Mn single-atom ($\text{Mn}_{\text{SAC-N-C}}$), Mn single-atom coupled Mn cluster ($\text{Mn}_{\text{cluster}}/\text{Mn}_{\text{SAC-N-C}}$), Mn-Mn dual-single-atom ($\text{Mn}_{\text{DAC-N-C}}$), and Mn-Mn dual single-atom coupled Mn cluster ($\text{Mn}_{\text{cluster}}/\text{Mn}_{\text{DAC-N-C}}$), were established for density functional theory (DFT) calculations (Fig. S1a-d). We found that the bond lengths of the four Mn-N coordination sites in $\text{Mn}_{\text{SAC-N-C}}$ were equal (1.9 Å) (Fig. S1a), which matched the D_{4h} symmetry of MnN_4 [40]. In the double single-atom $\text{Mn}_{\text{DAC-N-C}}$ (Fig. S1b), two types of Mn-N bond lengths were recorded: one (1.97 Å) was for the Mn-N bond coordinated to one Mn atom, and the other (1.82 Å) was for the Mn-N bond coordinated to two Mn atoms, which was smaller than that of the Mn-N bond

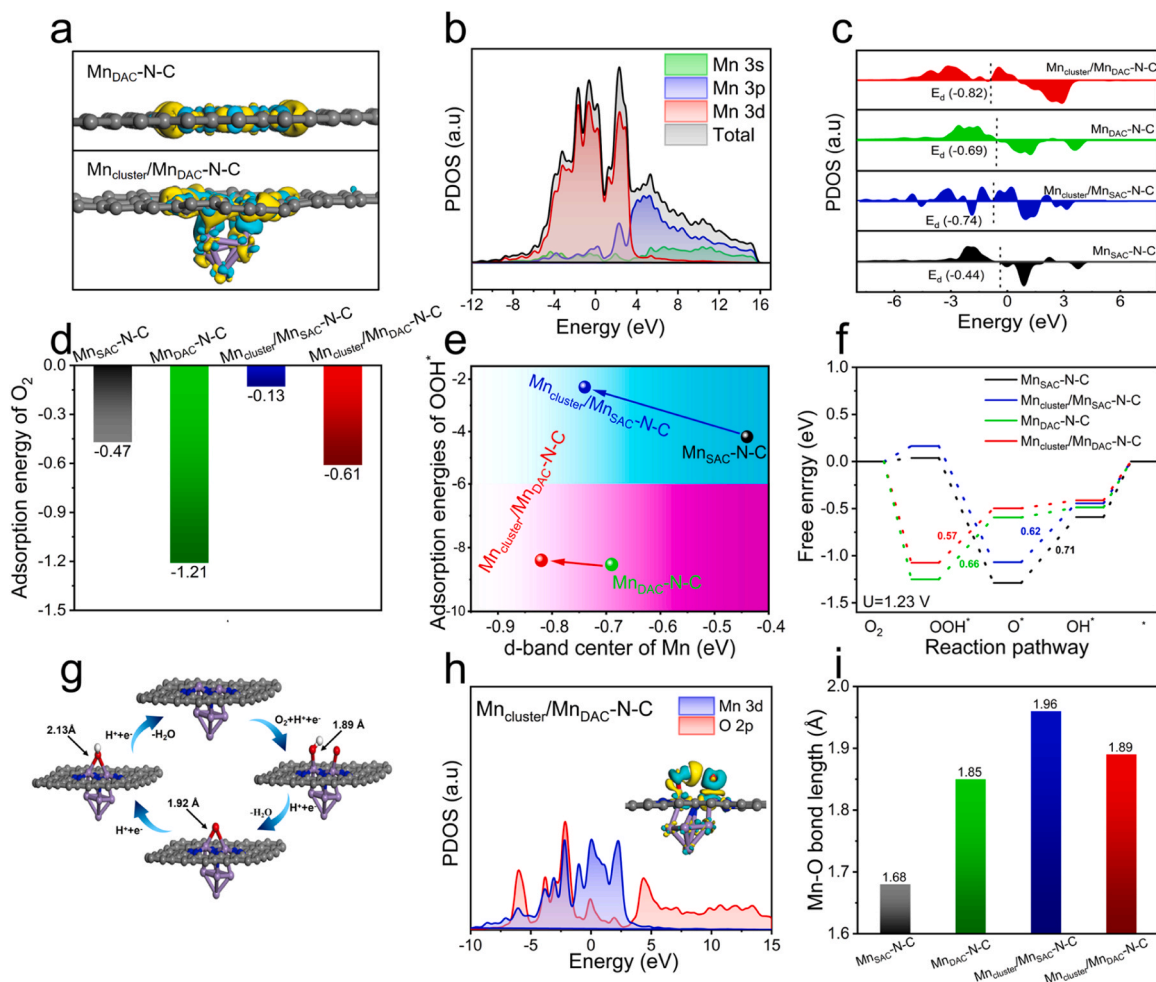


Fig. 1. (a) The difference in charge density between $\text{Mn}_{\text{DAC-N-C}}$ and $\text{Mn}_{\text{cluster}}/\text{Mn}_{\text{DAC-N-C}}$. (b) PDOS curves of Mn in $\text{Mn}_{\text{cluster}}/\text{Mn}_{\text{DAC-N-C}}$. (c, d) The d band center and O_2 adsorption energy of $\text{Mn}_{\text{SAC-N-C}}$, $\text{Mn}_{\text{cluster}}/\text{Mn}_{\text{SAC-N-C}}$, $\text{Mn}_{\text{DAC-N-C}}$ and $\text{Mn}_{\text{cluster}}/\text{Mn}_{\text{DAC-N-C}}$. (e) Relationships between OOH^* adsorption energies and d band centers. (f) ORR free energy diagrams at $U = 1.23$ V. (g) Complete $4e^-$ ORR path for $\text{Mn}_{\text{cluster}}/\text{Mn}_{\text{DAC-N-C}}$. (h) PDOS curves of OOH^* in $\text{Mn}_{\text{cluster}}/\text{Mn}_{\text{DAC-N-C}}$. (i) Mn-O bond length in OOH^* .

in $\text{Mn}_{\text{SAC-N-C}}$. A shorter bond length indicates greater stability of the bond; thus, $\text{Mn}_{\text{DAC-N-C}}$ may have a more stable structure.

A comparison of the calculated formation energies (Table S1), revealed that the double single-atom $\text{Mn}_{\text{DAC-N-C}}$ had the lowest formation energy, which indicated that the double-nucleated $\text{Mn}_{\text{DAC-N-C}}$ was easier to form and more stable than the single-nucleated $\text{Mn}_{\text{SAC-N-C}}$ was [41]. When Mn clusters were introduced, the bond lengths of all the Mn-N bonds in the $\text{Mn}_{\text{cluster}}/\text{Mn}_{\text{SAC-N-C}}$ and $\text{Mn}_{\text{cluster}}/\text{Mn}_{\text{DAC-N-C}}$ structures increased (Fig. S1c-d), which might be attributed to the distortion of the geometry of the MnN_4 center by the introduction of clusters (Fig. S2a-d) and a slight decrease in the formation energy. The differential distributions of the charge density (Fig. 1a and Fig. S3) showed that the electronic structures around $\text{Mn}_{\text{SAC-N-C}}$ and $\text{Mn}_{\text{DAC-N-C}}$ were redistributed after the Mn clusters were introduced, which indicated that electron transfer occurred between the MnN_4 (or $\text{Mn}_2\text{-N}_6$) sites and the Mn clusters. To investigate the role of the out-of-nuclear electrons of Mn in catalysis, we constructed a PDOS diagram of the electron orbital distribution of Mn (Fig. 1b). The results showed that the electrons in the 3d orbital of Mn contributed the most to the overall performance, indicating that the ORR performance was mainly enhanced by the electrons in the 3d orbital of Mn in the catalyst. Upon synergizing the Mn clusters in $\text{Mn}_{\text{SAC-N-C}}$ and $\text{Mn}_{\text{DAC-N-C}}$, the d-electron state of Mn changed, and the d-band center showed a negative shift (Fig. 1c). These changes also indicated that electron transfer occurred between the Mn clusters and MnN_4 [30,42]. Additionally, the adsorption energies of O_2 and OOH^* on the different catalysts were separately calculated (Fig. 1d and Fig. S4), and it was found that $\text{Mn}_{\text{DAC-N-C}}$ had two Mn active sites and that O_2 was adsorbed on it in a bridging manner (Fig. S5). The two active sites were connected to both ends of the O_2 molecule, and the O-O bond broke during adsorption, forming two O^* . This kind of binuclear adsorption is more likely to occur than mononuclear adsorption of O_2 [43], solve the problem of difficulty in oxygen adsorption by Mn-based single-atom catalysts. Fig. 1e shows the correlation between the OOH^* adsorption energy and the d band center for the $\text{Mn}_{\text{SAC-N-C}}$, $\text{Mn}_{\text{DAC-N-C}}$, $\text{Mn}_{\text{cluster}}/\text{Mn}_{\text{SAC-N-C}}$, and $\text{Mn}_{\text{cluster}}/\text{Mn}_{\text{DAC-N-C}}$ structures. The structural evolution from a single nucleus to a double nucleus and from a cluster-less to a clustered state led to a decrease in the d-band center and the adsorption energy of OOH^* , which indicated that the d-electronic state of the active site Mn changed.

The changes in the free energy of $\text{Mn}_{\text{SAC-N-C}}$, $\text{Mn}_{\text{cluster}}/\text{Mn}_{\text{SAC-N-C}}$, $\text{Mn}_{\text{DAC-N-C}}$, and $\text{Mn}_{\text{cluster}}/\text{Mn}_{\text{DAC-N-C}}$ at each step of the ORR process ($U = 1.23 \text{ V}$) are shown in Fig. 1f and Table S2. Adsorbing O_2 molecules and coupling a proton in the first step of the ORR in $\text{Mn}_{\text{SAC-N-C}}$ and $\text{Mn}_{\text{cluster}}/\text{Mn}_{\text{SAC-N-C}}$ were endothermic processes, suggesting that these reactions cannot occur spontaneously at the catalyst surface, which is detrimental to the overall ORR occurrence. In contrast, for $\text{Mn}_{\text{DAC-N-C}}$ and $\text{Mn}_{\text{cluster}}/\text{Mn}_{\text{DAC-N-C}}$, the first step was exothermic because the double-site bridging adsorption facilitated oxygen adsorption. Additionally, the rate-determining step (RDS) of $\text{Mn}_{\text{DAC-N-C}}$ was the second step (OOH^* to O^*). After Mn clusters were introduced, due to the decrease in the adsorption of OH^* , the reaction energy barrier in this step decreased, thereby accelerating the ORR. Schematic diagrams (Fig. 1g and Fig. S6–9) of the dynamic changes in the bond lengths of OOH^* , O^* , and OH^* in the ORR pathway for $\text{Mn}_{\text{SAC-N-C}}$, $\text{Mn}_{\text{cluster}}/\text{Mn}_{\text{SAC-N-C}}$, $\text{Mn}_{\text{DAC-N-C}}$, and $\text{Mn}_{\text{cluster}}/\text{Mn}_{\text{DAC-N-C}}$ were calculated separately, and the change in free energy in each step of the ORR at 0 V was recorded. The ORR at these four active sites could occur naturally at 0 V. The changes in the bond lengths of OOH^* , O^* , and OH^* showed the adsorption state between the active site and the intermediates to some extent [44,45].

To further explain the adsorption state of oxygen-containing intermediates during the ORR, we calculated the differential charge density of OOH^* for the four structural models and constructed a PDOS diagram of the active site Mn and the 2p orbitals of the O attached to it (Fig. 1h and Fig. S10). The charge density distributions between Mn and O in the different structural models were different. For example, the electron distribution between Mn and O in $\text{Mn}_{\text{SAC-N-C}}$ was significantly

greater than that in $\text{Mn}_{\text{cluster}}/\text{Mn}_{\text{SAC-N-C}}$, which indicated that the interaction between Mn and O at the active site was weakened and that the Mn-O bond length increased after the Mn clusters were introduced (Fig. 1i). Thus, the binding strength of $\text{Mn}_{\text{cluster}}/\text{Mn}_{\text{SAC-N-C}}$ to OOH^* was weaker than that of $\text{Mn}_{\text{SAC-N-C}}$, and the binding strength of $\text{Mn}_{\text{cluster}}/\text{Mn}_{\text{DAC-N-C}}$ to OOH^* was weaker than that of $\text{Mn}_{\text{DAC-N-C}}$ [24]. The difference was that the oxygen adsorbed by $\text{Mn}_{\text{SAC-N-C}}$ and $\text{Mn}_{\text{cluster}}/\text{Mn}_{\text{SAC-N-C}}$ was terminal, whereas $\text{Mn}_{\text{DAC-N-C}}$ and $\text{Mn}_{\text{cluster}}/\text{Mn}_{\text{DAC-N-C}}$ exhibited bridging. Thus, in the ORR process on $\text{Mn}_{\text{DAC-N-C}}$ and $\text{Mn}_{\text{cluster}}/\text{Mn}_{\text{DAC-N-C}}$, the rate-determining step (RDS) is the desorption of OH^* during the conversion of OOH^* to O^* (Fig. 1g). As the introduction of Mn clusters led to an asymmetric distortion of the $\text{Mn}_2\text{-N}_6$ planar structure to some extent (Fig. S2a-d), which resulted in a non-uniform distribution of electrons around the active site Mn, the adsorption intensities of the oxygen-containing intermediates adsorbed on different Mn sites were slightly different during the ORR.

To summarize, it can be concluded that the oxygen adsorption capacity of $\text{Mn}_{\text{DAC-N-C}}$ was considerably greater than that of $\text{Mn}_{\text{SAC-N-C}}$ due to the unique bridging adsorption mode. After Mn clusters were introduced, due to the disruption of the planar structure of $\text{Mn}_{\text{DAC-N-C}}$, the electron configuration around the active sites was further altered, and the adsorption strength of oxygen-containing intermediates decreased during the ORR process and accelerated the ORR, thus showing excellent ORR performance.

3.2. Synthesis and structural characterization of the $\text{Mn}_{\text{cluster}}/\text{Mn}_{\text{DAC-N-C}}$ catalysts

Based on the predicted results of theoretical calculations, a novel and simple strategy was used to synthesize $\text{Mn}_{\text{cluster}}/\text{Mn}_{\text{DAC-N-C}}$ catalysts by secondary carbonation; these catalysts are composed mainly of Mn clusters and double single-atom $\text{Mn}_2\text{-N}_6$ configurations, as proven in the following characterization results. The preparation of the $\text{Mn}_{\text{cluster}}/\text{Mn}_{\text{DAC-N-C}}$ electrocatalyst is shown in Fig. 2. First, manganese chloride tetrahydrate and glycine in an aqueous solution were homogeneously mixed and dried to obtain the glycine-MnCl₂ precursor. Then, the glycine-MnCl₂ precursor was heat-treated at 900 °C in an atmosphere of nitrogen for 2 h to obtain an annealed product labeled $\text{MnO}/\text{Mn-N-C}$. Then, $\text{MnO}/\text{Mn-N-C}$ was acid-washed with HCl (1 mol/L) at room temperature for 6 h to remove MnO and unstable Mn species to obtain $\text{Mn}_{\text{DAC-N-C}}$. Finally, $\text{Mn}_{\text{DAC-N-C}}$ was heat-treated again at 900 °C in an atmosphere of nitrogen for 2 h to obtain the final catalyst $\text{Mn}_{\text{cluster}}/\text{Mn}_{\text{DAC-N-C}}$.

To determine whether glycine was coordinated with MnCl_2 , the formation of glycine-MnCl₂ complexes was confirmed by X-ray diffraction (XRD) and Fourier transform infrared spectroscopy (FT-IR). The XRD results (Fig. S11a) for glycine-MnCl₂ showed that the characteristic peaks of glycine-MnCl₂ precursor obtained by mixing glycine with

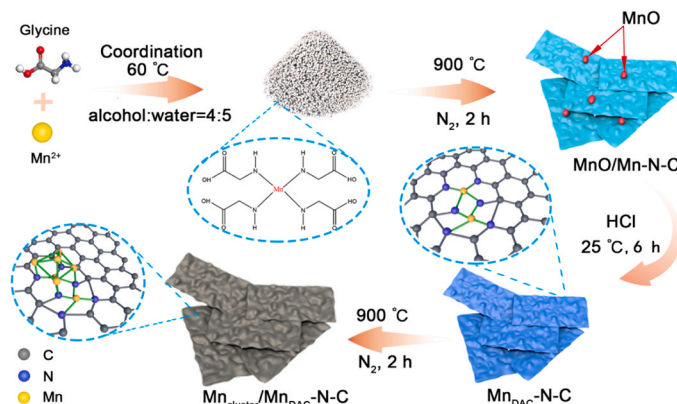


Fig. 2. Illustration of the synthesis process of the $\text{Mn}_{\text{cluster}}/\text{Mn}_{\text{DAC-N-C}}$ catalyst.

MnCl_2 were different from those of glycine and MnCl_2 . A new peak was generated near 11° , which indicated that a new species was formed. Additionally, the FT-IR spectra of glycine- MnCl_2 precursors (Fig. S11b) showed significant changes compared to those of glycine alone. In the infrared spectrum of glycine, the absorption peaks near 550 cm^{-1} , 2220 cm^{-1} , and 3170 cm^{-1} were related to the bending vibration of NH_3^+ in amino acids, indicating that intensity and displacement of these peaks changed significantly in the precursor of glycine- MnCl_2 . The N atom of the amino group in glycine was coordinated with the Mn in manganese chloride.

Field emission scanning electron microscopy (FE-SEM) and transmission electron microscopy (TEM) images (Fig. S12a-b) showed that the $\text{MnO}/\text{Mn-N-C}$ produced by annealing of glycine- MnCl_2 had prominent particles on the carbon substrate. The XRD results indicated that these particles were mostly composed of MnO , but a few were also composed of Mn (Fig. S12c). TEM images of $\text{Mn}_{\text{DAC-N-C}}$ (Fig. S13a-b) showed that no particles were present on the surface of the carbon substrate after acid washing. Aberration-corrected high-angle annular dark-field scanning transmission electron microscopy (AC-HAADF-STEM) of the $\text{Mn}_{\text{DAC-N-C}}$ showed that most of Mn was distributed as paired dual-nuclear single atoms on the surface of the carbon substrate, moreover, a few isolated Mn single atoms and Mn clusters (Fig. S13c-d) and C, N, and Mn were uniformly distributed on the carbon substrate (Fig. S13e). Diffraction peaks corresponding to MnO and Mn particles

were not found in the XRD spectrum (Fig. S13f), which indicated that MnO and unstable Mn particles on $\text{MnO}/\text{Mn-N-C}$ were removed after pickling. The SEM and TEM images of the $\text{Mn}_{\text{cluster}}/\text{Mn}_{\text{DAC-N-C}}$ catalyst are shown in Fig. 3a-b, where the catalyst had a loose flocculent structure. High-resolution TEM images of $\text{Mn}_{\text{cluster}}/\text{Mn}_{\text{DAC-N-C}}$ (Fig. 3c) showed an amorphous structure. The physical phase of the $\text{Mn}_{\text{cluster}}/\text{Mn}_{\text{DAC-N-C}}$ catalyst was further examined by XRD (Fig. 3d). We identified two prominent diffraction peaks centered at 26° and 44° that were attributed to the (002) and (101) planes of graphitic carbon, respectively. HAADF-STEM and corresponding elemental mapping images also confirmed the uniform dispersion of C, N, and Mn on the carbon carrier (Fig. 3e). The Mn content in $\text{Mn}_{\text{cluster}}/\text{Mn}_{\text{DAC-N-C}}$ was approximately 0.57 wt%, as determined via inductively coupled plasma emission spectrometry (ICP-OES) analysis (Table S3). To confirm the formation of $\text{Mn}_{\text{DAC-N-C}}$ and $\text{Mn}_{\text{cluster}}$, AC-HAADF-STEM was used analysis (Fig. 3f). The red dashed boxes indicate that the Mn dual-nuclear single-atom pairs were well-dispersed in the carbon substrate, the isolated single atoms are circled by small red dashed circles, and the regions encircled by yellow dashed circles indicate that Mn clusters existed in the catalyst. The number of clusters in the catalyst increased significantly after the second pyrolysis, compared with that in Fig. S13d, which was due to the migration of Mn atoms by high temperature pyrolysis. Moreover, these Mn dual-nuclear single atoms pairs and isolated Mn single atoms were distributed around the Mn cluster. The distance intensity distributions

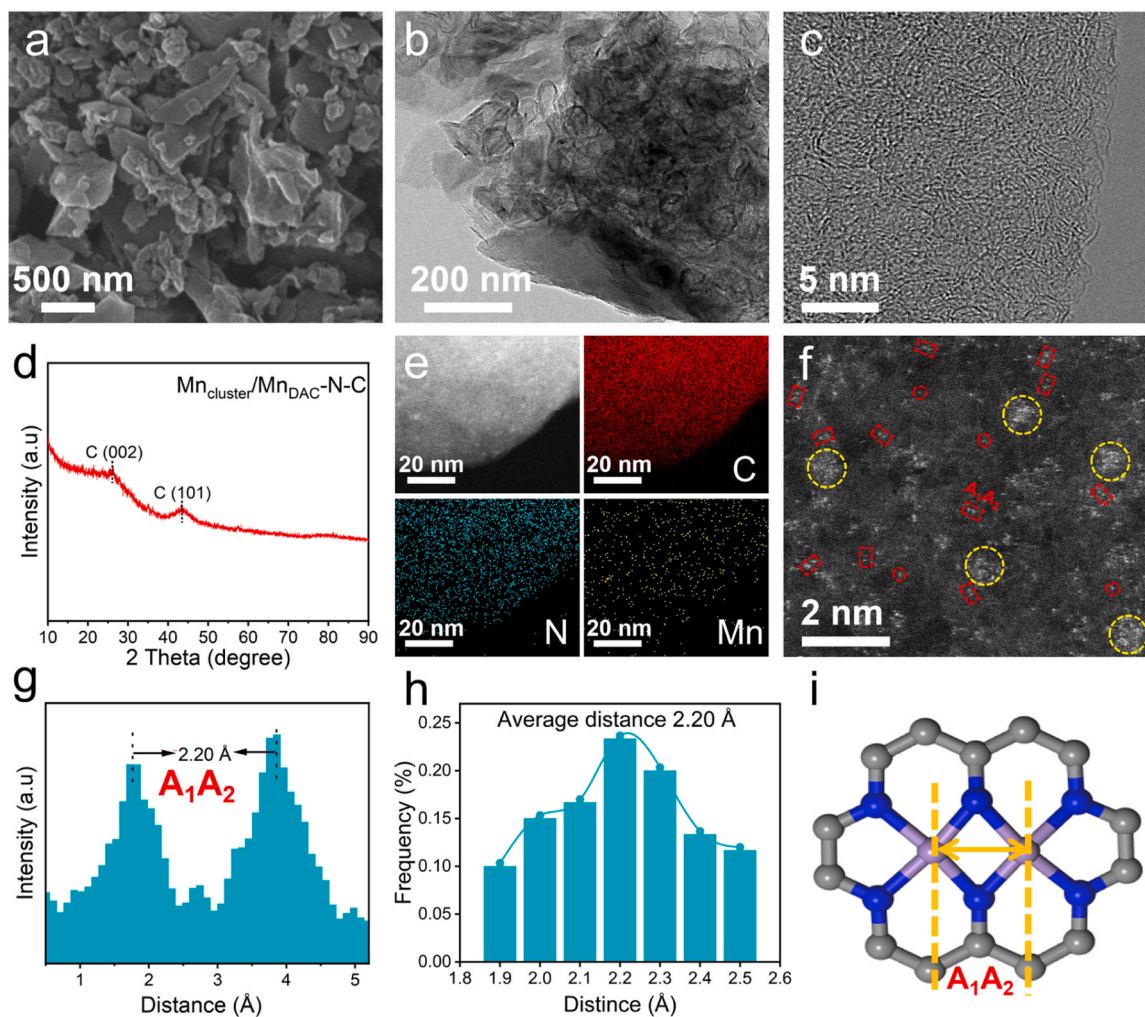


Fig. 3. (a) SEM image. (b, c) HR-TEM image, (d) XRD pattern, (e) EDS elemental mapping of $\text{Mn}_{\text{cluster}}/\text{Mn}_{\text{DAC-N-C}}$. (f) AC-HAADF-STEM image of $\text{Mn}_{\text{cluster}}/\text{Mn}_{\text{DAC-N-C}}$; some bimetallic Mn-Mn sites, isolated Mn single atoms and Mn clusters are highlighted in red and yellow. (g) The intensity profiles obtained for bimetallic Mn-Mn sites. (h) Statistical Mn-Mn distance in the observed diatomic pairs. (i) Structure diagram of $\text{Mn}_{\text{cluster}}/\text{Mn}_{\text{DAC-N-C}}$.

between the Mn-Mn pairs A_1A_2 labeled in Fig. 3f are shown in Fig. 3g. The distances between more than 100 Mn-Mn pairs supported on the carbon substrate were statistically analyzed (Fig. 3h and Fig. S14), which revealed an average distance of 2.2 Å between the Mn-Mn pairs. The average distance between the Mn-Mn pairs in the structural model of the Mn dual-core single-atoms obtained by theoretical calculations and simulations is shown in Fig. 3i. The distance between the Mn-Mn pairs (2.20 Å) was consistent with the experimental results. In addition, the AC-HAADF-STEM images of the prepared Mn_{SAC} -N-C and $Mn_{cluster}/Mn_{SAC}$ -N-C catalysts are shown in Fig. S15 and Fig. S16, which show that Mn in $Mn_{cluster}/Mn_{SAC}$ -N-C is mostly dispersed as a single Mn atom and that there are fewer Mn clusters; additionally, Mn_{SAC} -N-C is mostly dispersed as a single Mn atom.

In Fig. 4a, the Raman spectra of MnO/Mn -N-C, Mn_{DAC} -N-C, and $Mn_{cluster}/Mn_{DAC}$ -N-C show the characteristic disordered D-band (1334 cm^{-1}) and graphitic carbon-related G-band (1590 cm^{-1}). The I_D/I_G ratios for MnO/Mn -N-C, Mn_{DAC} -N-C, and $Mn_{cluster}/Mn_{DAC}$ -N-C were 1.05, 1.11, and 1.18, respectively. The variation in the I_D/I_G values indicates that pickling increases the degree of defects in the catalyst material, while the degree of defects in the catalyst material can be further enhanced by the subsequent step of secondary carbonization. Among them, $Mn_{cluster}/Mn_{DAC}$ -N-C has the most defective sites, and the defects in the catalyst are closely related to the distribution of active sites, which play a crucial role in the electrocatalytic ORR [46]. Moreover, the I_D/I_G of the $Mn_{cluster}/Mn_{SAC}$ -N-C catalyst obtained by halving Mn addition during the synthesis process is 0.73 (Fig. S17), corresponding to a significantly lower degree of defects, suggesting that the Mn content affects the defect sites in the catalyst material, which in turn affects the performance of the ORR.

The specific surface area of a catalyst strongly affects the distribution of active sites. A larger specific surface area of the catalyst indicates that more active sites are exposed, which can further enhance the ORR performance. Therefore, we performed BET-specific surface area tests on

the catalysts (Fig. 4b and Table S4). The BET-specific surface area of the $Mn_{cluster}/Mn_{DAC}$ -N-C catalysts was $1524\text{ m}^2\text{ g}^{-1}$, which was considerably greater than that reported in many studies on porous carbon-based ORR catalysts (Fig. 4c). The pore types in $Mn_{cluster}/Mn_{DAC}$ -N-C were mainly in the form of micropores and mesopores. The micropores favored the distribution of more active sites and the mesopores favored the mass transfer of ORR intermediates. Additionally, the BET-specific surface area of MnO/Mn -N-C was $960\text{ m}^2\text{ g}^{-1}$ (Fig. S18a-b); the BET-specific surface area increased significantly to $1521\text{ m}^2\text{ g}^{-1}$ after acid washing. This increase probably occurred because MnO and some unstable Mn species in the carbon substrate were removed by acid washing, which led to a significant increase in the specific surface area. To analyze the chemical states of C, N, and Mn in the catalyst, the $Mn_{cluster}/Mn_{DAC}$ -N-C catalyst was characterized by X-ray photoelectron spectroscopy (XPS). The high-resolution spectrum of C 1s is shown in Fig. 4d, and it could be fitted to three peaks by division, attributed to C-C/C=C (284.7 eV), C=C-N (285.6 eV) and O-C=O (289.8 eV) [47,48]. The high-resolution N 1s spectra were fitted to five peaks (Fig. 4e) for pyridinic-N (398.2 eV), Mn-N (399.3 eV), pyrrolic-N (400.8 eV), graphitic-N (401.9 eV), and oxidized-N (405.5 eV) [24,46]; the contents of different types of N are shown in Fig. 4f. These results showed that the N atoms were embedded in the carbon skeleton of the $Mn_{cluster}/Mn_{DAC}$ -N-C catalyst and coordinated with the Mn atoms. Compared to those of Mn_{DAC} -N-C, the $Mn_{cluster}/Mn_{DAC}$ -N-C sample exhibited a 2% increase in pyridinic-N content, a 1% increase in Mn-N content, no change in graphitic-N content, a 1% increase in oxidation-N content, and a 4% decrease in pyrrolic-N content (Fig. S24). An increase in the Mn-N content leads to an increase in the number of active sites, which is beneficial for the ORR. Pyridinic-N and graphitic-N have strong electron-donating abilities, which accelerate electron transfer and the ORR process [49]. Among all the compared catalysts, $Mn_{cluster}/Mn_{DAC}$ -N-C has the highest content of Mn-N as an active site and the highest content of graphitic nitrogen. The results of the XPS analysis

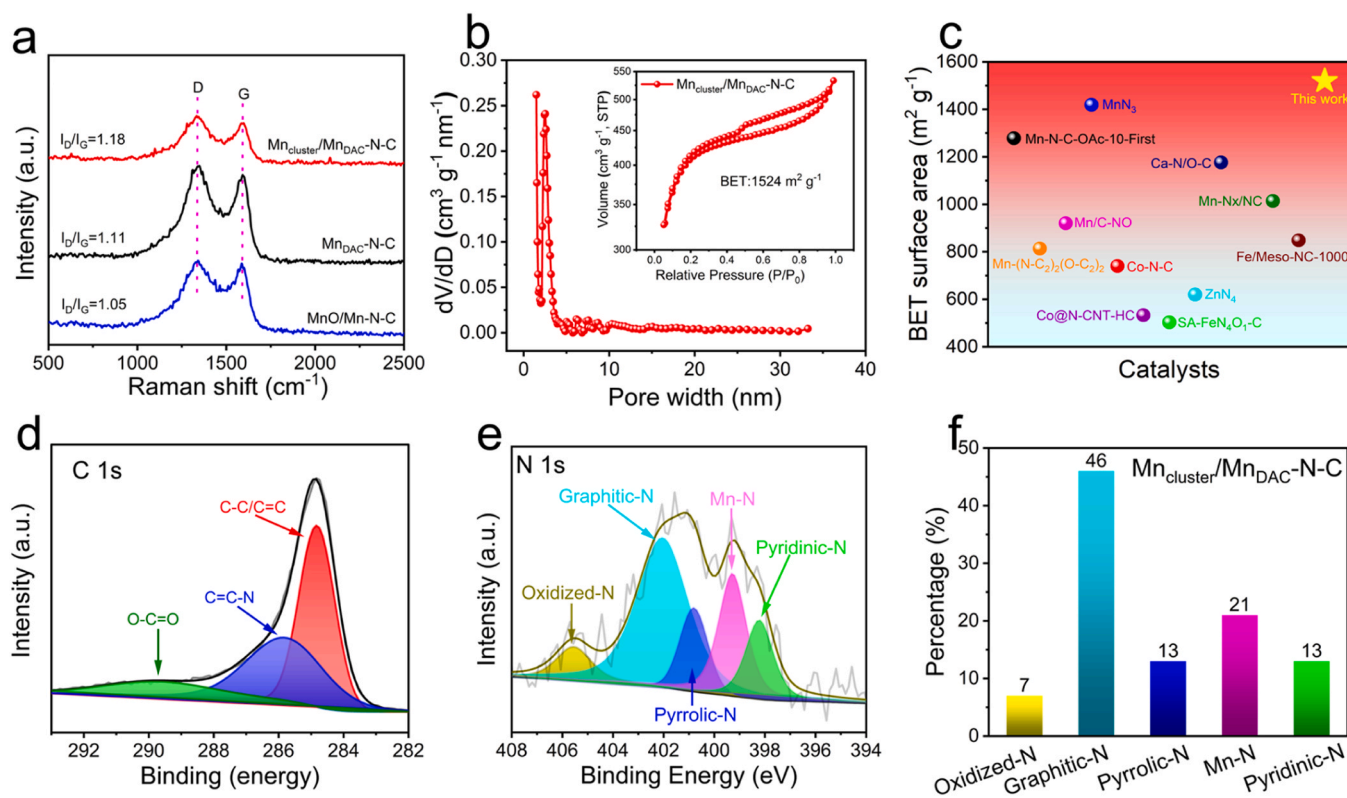


Fig. 4. (a) Raman spectra of MnO/Mn -N-C, Mn_{DAC} -N-C, and $Mn_{cluster}/Mn_{DAC}$ -N-C. (b) Nitrogen adsorption-desorption isotherms and pore size distributions of $Mn_{cluster}/Mn_{DAC}$ -N-C. (c) Comparison of the surface area of $Mn_{cluster}/Mn_{DAC}$ -N-C with that of other literature catalysts. (d, e) High-resolution C 1s and N 1s XPS spectra for $Mn_{cluster}/Mn_{DAC}$ -N-C. (f) The proportions of different N contents in $Mn_{cluster}/Mn_{DAC}$ -N-C.

corresponding to MnO/Mn-N-C, Mn_{DAC}-N-C, Mn_{cluster}/Mn_{SAC}-N-C, and Mn_{SAC}-N-C are shown in Fig. S19-Fig. S24. The Mn²⁺ and Mn³⁺ peaks were observed in the high-resolution Mn 2p spectra of MnO/Mn-N-C, and were attributed to the coordination of MnO and Mn with N [26,37].

Since the Mn content in Mn_{DAC}-N-C and Mn_{cluster}/Mn_{DAC}-N-C is too low to observe the signal of Mn 2p in high-resolution XPS spectra, the chemical state of Mn in Mn_{DAC}-N-C and Mn_{cluster}/Mn_{DAC}-N-C cannot be further analyzed by XPS. Similarly, the chemical state of Mn in Mn_{SAC}-N-C and Mn_{cluster}/Mn_{SAC}-N-C, which contains even less Mn, could not be further analyzed by XPS.

To determine the detailed structure of the Mn atoms in the catalyst, the coordination environment of Mn in the catalyst was further investigated by X-ray absorption near edge structure (XANES) and extended X-ray absorption fine spectroscopy (EXAFS). The K-edge XANES spectra of Mn_{cluster}/Mn_{DAC}-N-C, Mn₂O₃, Mn foil, MnO, and MnPc are shown in Fig. 5a, where we found that the valence states of the Mn atoms of the Mn_{cluster}/Mn_{DAC}-N-C catalysts were between those of MnO (+2) and Mn₂O₃ (+3). The absorption edge of Mn_{cluster}/Mn_{DAC}-N-C shifted toward a higher energy than that of the Mn foil comparison sample, and this result indicated that the Mn atoms in Mn_{cluster}/Mn_{DAC}-N-C had a higher oxidation state than did those in the Mn foil. This phenomenon might be attributed to the increase in the valence state of the Mn atoms due to the coordination of nitrogen atoms with the Mn atoms in the Mn_{cluster}/Mn_{DAC}-N-C catalyst. As shown in the Fourier transform (FT) k³-weighted EXAFS spectrum of the Mn K-edge (Fig. 5b), the peak at 1.45 Å corresponding to the Mn-N bond in MnPc was attributed to Mn_{cluster}/Mn_{DAC}-N-C. No Mn-O bond corresponding to MnO was found near 1.62 Å, which indicated that the oxygen in the catalyst was not coordinated with Mn. Fig. 5b shows the appearance of the Mn-Mn characteristic peak of the Mn_{cluster}/Mn_{DAC}-N-C at 2.39 Å. However, there is a positive shift in this peak compare with Mn-foil because these clusters are partially coordinated with the C/N/O atoms of the carbon substrate. This suggests

that the valence state of Mn of the clusters in Mn_{cluster}/Mn_{DAC}-N-C is greater than 0. The EXAFS spectra of Mn_{cluster}/Mn_{DAC}-N-C were significantly different from those of MnO (Fig. S25a-b), and no absorption peak corresponding to the Mn-O bond was found near 500 cm⁻¹ in the FT-IR spectrum of Mn_{cluster}/Mn_{DAC}-N-C. These results also indicated that no coordination occurred between Mn and O, and Mn only coordinated with N [41]. The EXAFS wavelet transform (WT) map is an efficient way to distinguish between backscattered atoms. In the k-space of Mn_{cluster}/Mn_{DAC}-N-C, the maximum peak at 3.8 Å⁻¹ is attributed to Mn-N, while the second maximum peak at 5.3 Å⁻¹ can be attributed to Mn-Mn scattering (Fig. 5c). The Mn-Mn bond k value of Mn_{cluster}/Mn_{DAC}-N-C is shifted relative to the Mn-Mn bond k value of Mn-foil, which may be related to the difference in the coordination number of Mn-Mn between the Mn-foil and Mn atom clusters [34,49,50]. To further show that Mn was present as an N coordination and that a Mn-Mn bond might exist, the EXAFS curve was fitted and analyzed using quantitative least squares; the results are shown in Fig. 5d-e and Table S5. We found that the Mn atom was coordinated to four N atoms with an average bond length of 1.89 Å for the Mn-N bond, and the distance from another Mn was 2.8 Å. According to the AC-HAADF-STEM image (Fig. 3f), Mn-Mn pairs and Mn clusters were observed. We speculated that the Mn in the Mn_{cluster}/Mn_{DAC}-N-C catalyst may mainly exist as Mn₂-N₆ and Mn clusters in the carbon framework structure, as well as isolated Mn-N₄, which is different from the structure of M-N-C monatomic catalysts commonly reported in other studies.

To summarize, in this work, Mn double single atoms, Mn clusters, and Mn single atoms loaded on carbon substrates with a high specific surface area were synthesized by the secondary carbonization method. In the obtained catalyst, the Mn atoms are coordinated with N to form Mn₂-N₆ or MnN₄ structures distributed around Mn clusters.

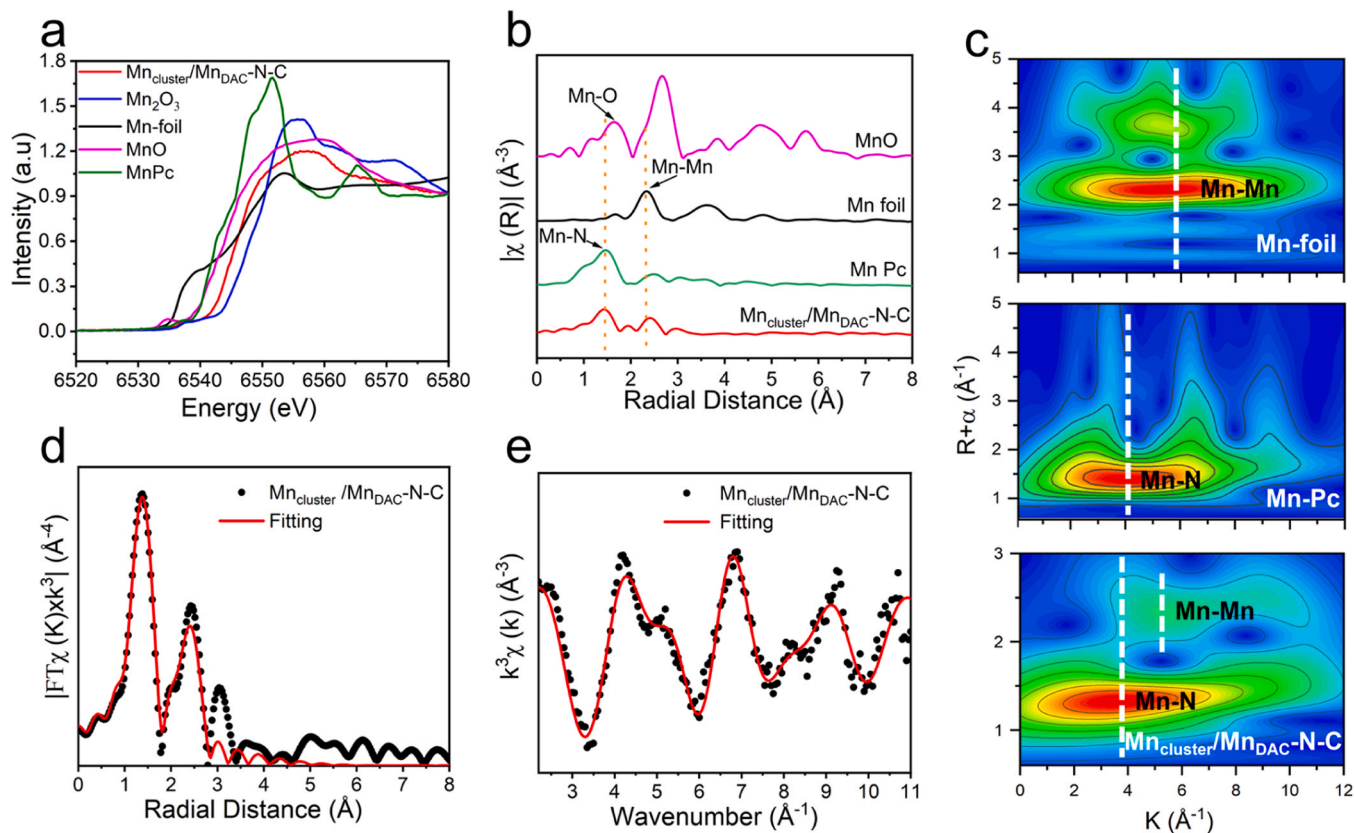


Fig. 5. (a) Mn K-edge XANES and (b) Fourier transform EXAFS spectra of Mn_{cluster}/Mn_{DAC}-N-C and reference samples. (c) EXAFS WT analysis. (d, e) EXAFS fitting curves of Mn_{cluster}/Mn_{DAC}-N-C in R space and K space.

3.3. ORR performance evaluation

The ORR performance of the catalysts was evaluated on a rotating disc electrode (RDE; 5 mm in diameter) using a typical three-electrode system in O_2 -saturated 0.1 M KOH and 0.1 M $HClO_4$. Our results were compared to the test results obtained for commercial Pt/C (20 wt%) and related control catalyst nitrogen-doped carbon materials N-C, MnO/Mn -N-C, and Mn_{DAC} -N-C. CV curves of the $Mn_{cluster}/Mn_{DAC}$ -N-C catalysts under N_2 saturation and O_2 saturation in 0.1 M KOH and 0.1 M $HClO_4$ are shown in Fig. S26a-b, respectively. We found a prominent reduction peak at 0.86 V (vs. RHE) in 0.1 M KOH, whereas, in 0.1 M $HClO_4$, the position of the reduction peak was at 0.68 V, which indicated that the $Mn_{cluster}/Mn_{DAC}$ -N-C catalyst had ORR activity under alkaline and acidic conditions. The LSV polarization curves of each catalyst in 0.1 M KOH at 1600 rpm are shown in Fig. 6a. $Mn_{cluster}/Mn_{DAC}$ -N-C exhibited the most positive onset potential of 1.00 V and a half-wave potential of 0.91 V, which were higher than the onset potential of 0.99 V and a half-wave

potential of 0.86 V for commercial Pt/C (Table S6). The half-wave potential under acidic conditions (0.1 M $HClO_4$) was close to the half-wave potential of commercial Pt/C (Fig. S27). Moreover, compared to that of the Mn_{DAC} -N-C catalyst, the catalytic performance of $Mn_{cluster}/Mn_{DAC}$ -N-C is significantly improved, which can be attributed to the introduction of Mn clusters during the second pyrolysis process. Moreover, from Fig. S28, it can be seen that the $E_{1/2}$ of $Mn_{cluster}/Mn_{DAC}$ -N-C (0.91 V) is superior to that of Mn_{DAC} -N-C (0.89 V), which is better than that of $Mn_{cluster}/Mn_{SAC}$ -N-C (0.86 V) and Mn_{SAC} -N-C (0.84 V), further indicating that the Mn double single-atom configuration coupled with Mn clusters in the $Mn_{cluster}/Mn_{DAC}$ -N-C catalyst is the most dominant active site. The kinetic current density (J_k) of $Mn_{cluster}/Mn_{DAC}$ -N-C was also the highest (Fig. 6b); it was 18.6 mA cm^{-2} at 0.85 V, which is 2.9 times greater than the J_k of commercial Pt/C (6.5 mA cm^{-2}). These results indicated that the cluster-regulated Mn-Mn double sites strongly influenced the increase in ORR activity. A comparison of the Tafel slopes of the catalyst is shown in Fig. 6c. We found that $Mn_{cluster}/Mn_{DAC}$ -N-C had

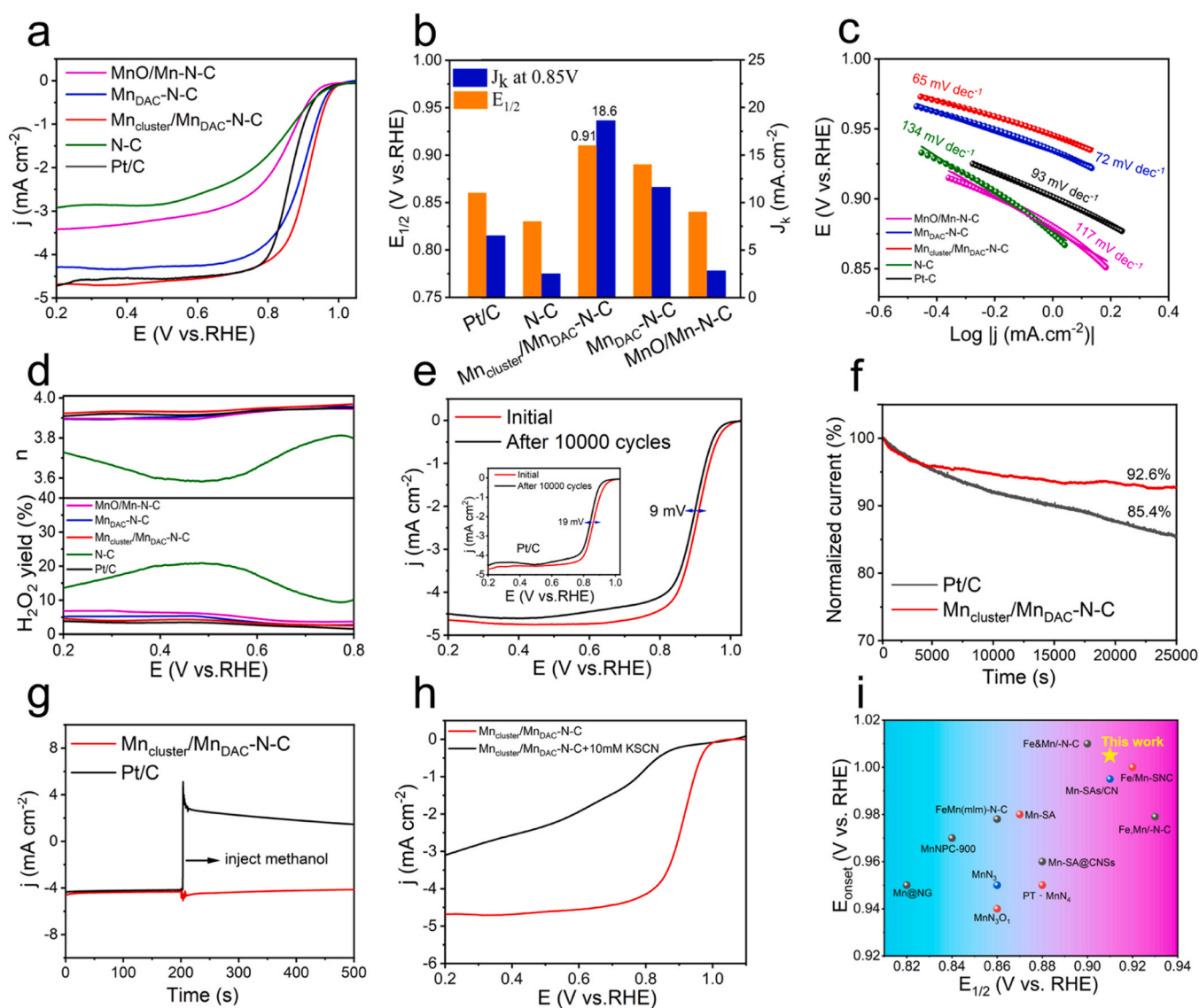


Fig. 6. (a) ORR LSV curves in O_2 -saturated 0.1 M KOH solution at 1600 rpm, (b) kinetic current density (J_k) at 0.85 V versus RHE and half-wave potentials and (c) Tafel plots of MnO/Mn-N-C, Mn_{DAC} -N-C, $Mn_{cluster}/Mn_{DAC}$ -N-C, N-C, and Pt/C. (d) The electron transfer number and hydrogen peroxide yield were obtained from the RRDE test. (e) LSV curves of $Mn_{cluster}/Mn_{DAC}$ -N-C before and after 10,000 CV cycles at a rotation rate of 1600 rpm; inset shows Pt/C. (f) Chronoamperometry test of the $Mn_{cluster}/Mn_{DAC}$ -N-C and Pt/C catalysts in alkaline media. (g) Methanol resistance test of $Mn_{cluster}/Mn_{DAC}$ -N-C, as characterized by chronoamperometric responses in 0.1 M KOH. (h) LSV curves in O_2 -saturated 0.1 M $HClO_4$ before and after the addition of 10 mM KSCN. (i) Comparison of the half-wave potential and onset potential of ORR catalysts.

the smallest Tafel slope and the best kinetic performance. The path type of ORR under alkaline conditions (0.1 M KOH) was investigated by rotating the ring-disk electrode (RRDE), as the $1e^-$ and $2e^-$ path-produced hydrogen peroxide products can corrode the polymer membrane of the fuel cell and decrease the cell lifetime. Therefore, the $4e^-$ path was the best for the ORR. As shown in Fig. 6d, the results for $Mn_{cluster}/Mn_{DAC}$ -N-C were the most satisfactory, with an average hydrogen peroxide yield of less than 5% and an average electron transfer number above 3.9, which indicated that the ORR process of the $Mn_{cluster}/Mn_{DAC}$ -N-C catalyst was mainly a four-electron reaction process. $Mn_{cluster}/Mn_{DAC}$ -N-C has a lower hydrogen peroxide yield than most Fe-based catalysts [4,19], which is an advantage that can extend the lifetime of the cell.

The electrochemically active specific surface area (ECSA) is a valuable parameter for evaluating the surface properties of a catalyst in an electrolyte environment, and is determined by measuring the catalyst's double layer capacitance (C_{dl}). The C_{dl} was calculated to be 85.6 mF cm^{-2} for $Mn_{cluster}/Mn_{DAC}$ -N-C, which exceeds that of $Mn_{cluster}/Mn_{SAC}$ -N-C (58.5 mF cm^{-2}), Mn_{DAC} -N-C (70.5 mF cm^{-2}) and Mn_{SAC} -N-C (40.9 mF cm^{-2}) (Fig. S29 and Fig. S30). Higher C_{dl} values indicate a greater density of active sites on the surface of the $Mn_{cluster}/Mn_{DAC}$ -N-C catalyst and faster ORR kinetics [46,47,51]. In addition, $Mn_{cluster}/Mn_{DAC}$ -N-C had the best kinetic current density normalized by the ECSA (Fig. S31) and the highest kinetic current density at 0.85 V (Table S7) compared to those of $Mn_{cluster}/Mn_{SAC}$ -N-C, Mn_{DAC} -N-C, and Mn_{SAC} -N-C, suggesting that $Mn_{cluster}/Mn_{DAC}$ -N-C has the highest intrinsic activity [50]. We calculated the turnover frequency (TOF) [40] at 0.85 V for $Mn_{cluster}/Mn_{DAC}$ -N-C, Mn_{DAC} -N-C and Pt/C, which have the best catalytic performance. The results (Fig. S32) showed that the TOF of $Mn_{cluster}/Mn_{DAC}$ -N-C was $3.1 \text{ e s}^{-1} \text{ sites}^{-1}$, which was higher than that of Mn_{DAC} -N-C ($2.6 \text{ e s}^{-1} \text{ sites}^{-1}$), further suggesting that the introduction of clusters significantly enhanced the catalyst performance.

Since the stability of the catalyst also plays an important role in determining practical applications, we investigated the cycling stability of $Mn_{cluster}/Mn_{DAC}$ -N-C with commercial Pt/C under alkaline conditions (Fig. 6e). After 10,000 electrochemical cyclic voltammetry tests at potentials ranging from 0.6 V to 1.0 V in O_2 -saturated 0.1 M KOH solution, we found that the loss of half-wave potential ($E_{1/2}$) of $Mn_{cluster}/Mn_{DAC}$ -N-C was only 9 mV, while the commercial Pt/C catalyst lost 19 mV of half-wave potential ($E_{1/2}$) after 10,000 electrochemical cycle voltammetry tests. Moreover, we tested the ORR performance of $Mn_{cluster}/Mn_{DAC}$ -N-C after six months of storage (Fig. S33). After six months, the half-wave potential of $Mn_{cluster}/Mn_{DAC}$ -N-C decayed by only 7 mV, and the limiting current density only slightly decreased. These results indicate that the $Mn_{cluster}/Mn_{DAC}$ -N-C catalyst material is relatively stable and suitable for practical applications. Additionally, we conducted a chronoamperometry test for the $Mn_{cluster}/Mn_{DAC}$ -N-C catalyst at a constant potential of 0.6 V (vs. RHE) (Fig. 6f) and found that the $Mn_{cluster}/Mn_{DAC}$ -N-C catalyst retained 92.6% of the initial current density after 25,000 s, while the commercial Pt/C catalyst only retained 85.4% of the initial current density. These findings suggested that $Mn_{cluster}/Mn_{DAC}$ -N-C had better ORR stability than Pt/C. To evaluate the tolerance of the $Mn_{cluster}/Mn_{DAC}$ -N-C catalyst to methanol crossover, we tested the *i*-t curves of $Mn_{cluster}/Mn_{DAC}$ -N-C and commercial Pt/C in 0.1 M KOH at an RDE rotation rate of 1600 rpm and compared them (Fig. 6g). After methanol was added to the test system at 200 s, the current density of Pt/C decreased sharply, but the current density of $Mn_{cluster}/Mn_{DAC}$ -N-C did not change significantly. These results indicated that the $Mn_{cluster}/Mn_{DAC}$ -N-C catalyst could resist methanol crossover and might be useful in direct methanol fuel cells. Moreover, in order to further verify that Mn_2-N_6 or $Mn-N_4$ are the active sites, a KSCN poisoning experiment was conducted on $Mn_{cluster}/Mn_{DAC}$ -N-C (Fig. 6h). After KSCN was added, the activity of the catalyst was basically completely lost, indicating that the metal site $Mn-N_x$ is the main active site in the $Mn_{cluster}/Mn_{DAC}$ -N-C catalyst. In addition, a comparison of the half-wave potentials of various types of single-atom catalysts reported in other published studies is shown in Fig. 6i and Table S8. We found that the $Mn_{cluster}/Mn_{DAC}$ -N-C

catalyst synthesized in this work exhibited remarkable ORR performance.

The OER performance was examined in an electrolyte of 1.0 M KOH. As shown in Fig. 7a, the $Mn_{cluster}/Mn_{DAC}$ -N-C catalyst exhibited an overpotential of 320 mV at 10 mA cm^{-2} , which was superior to that of commercial RuO_2 (340 mV) and pure nickel foam NF (420 mV). To determine the charge transfer resistance (R_{ct}), electrochemical impedance spectroscopy (EIS) was performed (Fig. S34). The $Mn_{cluster}/Mn_{DAC}$ -N-C catalyst exhibited the smallest charge transfer resistance ($R_{ct} = 0.51 \Omega$) among all the compared catalysts (Table S9), suggesting that $Mn_{cluster}/Mn_{DAC}$ -N-C has a better electron transfer rate and faster catalytic kinetics [51,52].

Considering that $Mn_{cluster}/Mn_{DAC}$ -N-C exhibited excellent electrochemical performance, we assembled a zinc-air battery, ZAB- $Mn_{cluster}/Mn_{DAC}$ -N-C, using $Mn_{cluster}/Mn_{DAC}$ -N-C as the cathode and Zn foil as the anode (Fig. 7b). The open circuit voltage (OCV) of ZAB- $Mn_{cluster}/Mn_{DAC}$ -N-C reached 1.48 V, which was higher than the OCV of the Pt/C+ RuO_2 assembled zinc-air battery (1.40 V) (Fig. 7c). The discharge-specific capacity of ZAB- $Mn_{cluster}/Mn_{DAC}$ -N-C at 10 mA cm^{-2} was 791 mAh g^{-1} , while that of commercial Pt/C+ RuO_2 was 779 mAh g^{-1} (Fig. 7d). Additionally, the peak power density of ZAB- $Mn_{cluster}/Mn_{DAC}$ -N-C was 180 mW cm^{-2} , which exceeded the peak power density of Pt/C+ RuO_2 (125 mW cm^{-2}) (Fig. 7e). Additionally, two ZAB- $Mn_{cluster}/Mn_{DAC}$ -N-C zinc-air batteries connected in series could light up a red LED (Fig. 7f). The stability of ZAB- $Mn_{cluster}/Mn_{DAC}$ -N-C was tested by charge discharge cycling (Fig. 7g-h). We found that ZAB- $Mn_{cluster}/Mn_{DAC}$ -N-C had high stability, and the charge discharge voltage difference was 1.02 V, which was lower than that of Pt/C+ RuO_2 (1.25 V) [53]. These results indicated that ZAB- $Mn_{cluster}/Mn_{DAC}$ -N-C had good charging and discharging ability. These results indicated that $Mn_{cluster}/Mn_{DAC}$ -N-C is a promising catalyst for application in zinc-air batteries.

4. Conclusion

In summary, a carbon nanosheet catalyst, $Mn_{cluster}/Mn_{DAC}$ -N-C, with a large specific surface area ($1524 \text{ m}^2 \text{ g}^{-1}$) was constructed by simultaneously loading Mn clusters, Mn homonuclear double single-atom Mn_2-N_6 structures and a few isolated Mn single atom. The DFT calculations showed that Mn_2-N_6 axially pulled by Mn clusters was the main active site, which presented a strong adsorption capacity for O_2 , and could rapidly capture O_2 during the ORR process. The Mn clusters can further modify the electronic distribution and geometric structure of Mn_2-N_6 . This process reduced the adsorption strength of the oxygen-containing intermediate at the active site and lowered the reaction energy barrier of the determining-rate step, thus enhancing the ORR performance. The $Mn_{cluster}/Mn_{DAC}$ -N-C catalyst exhibited excellent ORR performance under alkaline conditions ($E_{1/2} = 0.91 \text{ V}$), which was greater than that of commercial Pt/C (0.86 V). In this work, the proposed strategy for breaking the planar structure of the Mn_2-N_6 site and decreasing the adsorption strength of oxygenated intermediates, provided new insights and ideas for rationally designing new single-atom electrocatalysts with efficient ORR performance.

CRedit authorship contribution statement

Yanrong Ren: Validation, Resources. **Yan Lin:** Formal analysis. **Xikun Yang:** Formal analysis. **Mingli Xu:** Writing – review & editing, Supervision, Resources, Project administration, Investigation, Funding acquisition. **GuangTao Luo:** Writing – review & editing, Writing – original draft, Methodology, Formal analysis, Data curation, Conceptualization. **Enze Zhu:** Validation, Formal analysis, Data curation. **Chaoyang Shi:** Resources, Data curation.

Declaration of Competing Interest

The authors declare that they have no known competing financial

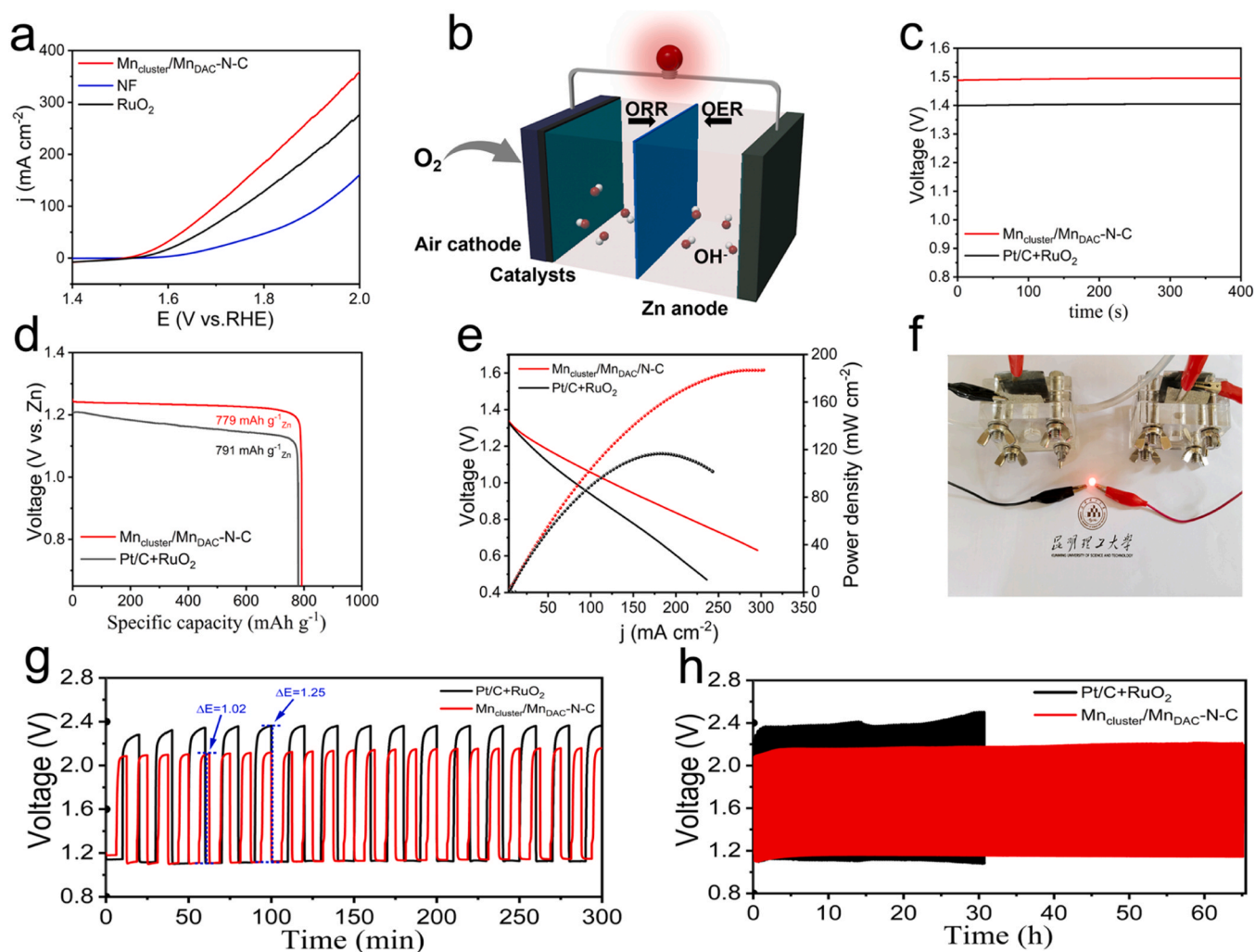


Fig. 7. (a) OER LSV curves. (b) Schematic diagram of the ZAB. Electrochemical characterization of the zinc-air battery (ZAB): (c) Open-circuit potentials (OCs) of $\text{Mn}_{\text{cluster}}/\text{Mn}_{\text{DAC}}\text{-N-C}$ and $\text{Pt/C} + \text{RuO}_2$. (d) Galvanostatic discharge curves of $\text{Mn}_{\text{cluster}}/\text{Mn}_{\text{DAC}}\text{-N-C}$ and $\text{Pt/C} + \text{RuO}_2$. (e) Polarization and power density curves of $\text{Mn}_{\text{cluster}}/\text{Mn}_{\text{DAC}}\text{-N-C}$ and $\text{Pt/C} + \text{RuO}_2$. (f) Photograph of a red LED powered by two liquid Zn-air batteries with $\text{Mn}_{\text{cluster}}/\text{Mn}_{\text{DAC}}\text{-N-C}$ as the air cathode. (g) Initial 5 h charge-discharge cycling curves of $\text{Mn}_{\text{cluster}}/\text{Mn}_{\text{DAC}}\text{-N-C}$ and $\text{Pt/C} + \text{RuO}_2$ at 7.8 mA. (h) ZAB durability tests at constant current density of 7.8 mA cm^{-2} .

interests or personal relationships that could have appeared to influence the work reported in this paper.

Data availability

Data will be made available on request.

Acknowledgements

This work was financially supported by the National Natural Science Foundation of China (No. 51764030), the Major Science and Technology Projects in Yunnan Province (202102AB080007), the Natural Science Foundation of Yunnan Province (202001AS070010), the Analysis and Testing Foundation of Kunming University of Science and Technology. We also thank Shiyanjia Lab (www.shiyanjia.com) for material characterizations and instrumentation support.

Appendix A. Supporting information

Supplementary data associated with this article can be found in the online version at [doi:10.1016/j.apcatb.2024.123939](https://doi.org/10.1016/j.apcatb.2024.123939).

References

- [1] Y. Wang, H. Su, Y. He, L. Li, S. Zhu, H. Shen, P. Xie, X. Fu, G. Zhou, C. Feng, D. Zhao, F. Xiao, X. Zhu, Y. Zeng, M. Shao, S. Chen, G. Wu, J. Zeng, C. Wang, Advanced electrocatalysts with single-metal-atom active sites, *Chem. Rev.* 120 (2020) 12217–12314, <https://doi.org/10.1021/acs.chemrev.0c00594>.
- [2] J. Zhang, H. Yang, B. Liu, Coordination engineering of single-atom catalysts for the oxygen reduction reaction: a review, *Adv. Energy Mater.* 11 (2021) 2002473, <https://doi.org/10.1002/aenm.202002473>.
- [3] C. Hao, Z. Liu, W. Liu, Y. Shi, Research progress of carbon-supported metal single atom catalysts for oxygen reduction reaction, *J. Inorg. Mater.* 36 (2021) 820, <https://doi.org/10.15541/jim20200582>.
- [4] Q. Ma, H. Jin, J. Zhu, Z. Li, H. Xu, B. Liu, Z. Zhang, J. Ma, S. Mu, Stabilizing Fe-N-C catalysts as model for oxygen reduction reaction, *Adv. Sci.* 8 (2021) 2102209, <https://doi.org/10.1002/advsc.202102209>.
- [5] Y. Wang, L. Wang, H. Fu, Research progress of Fe-N-C catalysts for the electrocatalytic oxygen reduction reaction, *Sci. China Mater.* 65 (2022) 1701–1722, <https://doi.org/10.1007/s40843-022-2059-x>.
- [6] L. Sun, Q. Gu, Y. Yang, H. Wang, J. Yu, X. Zhou, Two-dimensional transition metal dichalcogenides for electrocatalytic oxygen reduction reaction, *J. Inorg. Mater.* 37 (2022) 697, <https://doi.org/10.15541/jim20220128>.
- [7] L. Zhang, L. Xue, B. Lin, Q. Zhao, S. Wan, Y. Wang, H. Jia, H. Xiong, Noble metal single-atom catalysts for the catalytic oxidation of volatile organic compounds, *ChemSusChem* 15 (2022), <https://doi.org/10.1002/cssc.202200356>.
- [8] M. Xiao, J. Zhu, L. Ma, Z. Jin, J. Ge, X. Deng, Y. Hou, Q. He, J. Li, Q. Jia, S. Mukerjee, R. Yang, Z. Jiang, D. Su, C. Liu, W. Xing, Microporous framework induced synthesis of single-atom dispersed Fe-N-C Acidic ORR catalyst and its in situ reduced Fe-N₄ active site identification revealed by x-ray absorption spectroscopy, *ACS Catal.* 8 (2018) 2824–2832, <https://doi.org/10.1021/acscatal.8b00138>.

- [9] N. Yang, L. Li, J. Li, W. Ding, Z. Wei, Modulating the oxygen reduction activity of heteroatom-doped carbon catalysts via the triple effect: charge, spin density and ligand effect, *Chem. Sci.* 9 (2018) 5795–5804, <https://doi.org/10.1039/C8SC01801D>.
- [10] G. Zhang, Y. Jia, C. Zhang, X. Xiong, K. Sun, R. Chen, W. Chen, Y. Kuang, L. Zheng, H. Tang, W. Liu, J. Liu, X. Sun, W.-F. Lin, H. Dai, A general route via formamide condensation to prepare atomically dispersed metal–nitrogen–carbon electrocatalysts for energy technologies, *Energy Environ. Sci.* 12 (2019) 1317–1325, <https://doi.org/10.1039/C9EE00162J>.
- [11] X. Meng, D. Yang, S. Wang, X. Liu, W. Wang, A high performance ORR electrocatalyst—Mn–N₅–C/G: design, synthesis, and related mechanism, *Ionics* 27 (2021) 3489–3499, <https://doi.org/10.1007/s11581-021-04154-2>.
- [12] J. Wang, J. Kim, S. Choi, H. Wang, J. Lim, A review of carbon-supported nonprecious metals as energy-related electrocatalysts, *Small Methods* 4 (2020) 2000621, <https://doi.org/10.1002/smt.202000621>.
- [13] Y. Wang, H. Su, Y. He, L. Li, S. Zhu, H. Shen, P. Xie, X. Fu, G. Zhou, C. Feng, D. Zhao, F. Xiao, X. Zhu, Y. Zeng, M. Shao, S. Chen, G. Wu, J. Zeng, C. Wang, Advanced electrocatalysts with single-metal-atom active sites, *Chem. Rev.* 120 (2020) 12217–12314, <https://doi.org/10.1021/acs.chemrev.0c00594>.
- [14] W. Li, B. Liu, D. Liu, P. Guo, J. Liu, R. Wang, Y. Guo, X. Tu, H. Pan, D. Sun, F. Fang, R. Wu, Alloying Co species into ordered and interconnected macroporous carbon polyhedra for efficient oxygen reduction reaction in rechargeable zinc–air batteries, *Adv. Mater.* 34 (2022) 2109605, <https://doi.org/10.1002/adma.202109605>.
- [15] L. Bai, Z. Duan, X. Wen, R. Si, J. Guan, Atomically dispersed manganese-based catalysts for efficient catalysis of oxygen reduction reaction, *Appl. Catal. B: Environ.* 257 (2019) 117930, <https://doi.org/10.1016/j.apcatb.2019.117930>.
- [16] J. Huo, X. Cao, Y. Tian, L. Li, J. Qu, Y. Xie, X. Nie, Y. Zhao, J. Zhang, H. Liu, Atomically dispersed Mn atoms coordinated with N and O within an N-doped porous carbon framework for boosted oxygen reduction catalysis, *Nanoscale* 15 (2023) 5448–5457, <https://doi.org/10.1039/D2NR06096E>.
- [17] Z. Kong, T. Liu, K. Hou, L. Guan, Atomically dispersed Mn–N₄ electrocatalyst with high oxygen reduction reaction catalytic activity from metal–organic framework ZIF-8 by minimal-water-assisted mechanochemical synthesis, *J. Mater. Chem. A* 10 (2022) 2826–2834, <https://doi.org/10.1039/D1TA09183B>.
- [18] L. Zong, F. Lu, W. Zhang, K. Fan, X. Chen, B. Johannessen, D. Qi, N.M. Bedford, M. Warren, C.U. Segre, P. Liu, L. Wang, H. Zhao, Atomically-dispersed Mn-(N–C)₂(O–C)₂ sites on carbon for efficient oxygen reduction reaction, *Energy Storage Mater.* 49 (2022) 209–218, <https://doi.org/10.1016/j.ensm.2022.04.016>.
- [19] L. Peng, J. Yang, Y. Yang, F. Qian, Q. Wang, D. Sun–Waterhouse, L. Shang, T. Zhang, G.I.N. Waterhouse, Mesopore-rich Fe–N–C catalyst with FeN₄–O–NC single-atom sites delivers remarkable oxygen reduction reaction performance in alkaline media, *Adv. Mater.* 34 (2022) 2202544, <https://doi.org/10.1002/adma.202202544>.
- [20] L. Liu, A. Corma, Bimetallic sites for catalysis: from binuclear metal sites to bimetallic nanoclusters and nanoparticles, *acs.chemrev.*2c0073, *Chem. Rev.* (2023) 3, <https://doi.org/10.1021/acs.chemrev.2c00733>.
- [21] L. Li, K. Yuan, Y. Chen, Breaking the scaling relationship limit: from single-atom to dual-atom catalysts, *Acc. Mater. Res.* 3 (2022) 584–596, <https://doi.org/10.1021/accountsmr.1c00264>.
- [22] Z. Chen, X. Liao, C. Sun, K. Zhao, D. Ye, J. Li, G. Wu, J. Fang, H. Zhao, J. Zhang, Enhanced performance of atomically dispersed dual-site Fe–Mn electrocatalysts through cascade reaction mechanism, *Appl. Catal. B: Environ.* 288 (2021) 120021, <https://doi.org/10.1016/j.apcatb.2021.120021>.
- [23] Y. Wu, C. Ye, L. Yu, Y. Liu, J. Huang, J. Bi, L. Xue, J. Sun, J. Yang, W. Zhang, X. Wang, P. Xiong, J. Zhu, Soft template-directed interlayer confinement synthesis of a Fe–Co dual single-atom catalyst for Zn–air batteries, *Energy Storage Mater.* 45 (2022) 805–813, <https://doi.org/10.1016/j.ensm.2021.12.029>.
- [24] G. Yang, J. Zhu, P. Yuan, Y. Hu, G. Qu, B.-A. Lu, X. Xue, H. Yin, W. Cheng, J. Cheng, W. Xu, J. Li, J. Hu, S. Mu, J.-N. Zhang, Regulating Fe–spin state by atomically dispersed Mn–N in Fe–N–C catalysts with high oxygen reduction activity, *Nat. Commun.* 12 (2021) 1734, <https://doi.org/10.1038/s41467-021-21919-5>.
- [25] R. Gao, J. Wang, Z.-F. Huang, R. Zhang, W. Wang, L. Pan, J. Zhang, W. Zhu, X. Zhang, C. Shi, J. Lim, J.-J. Zou, Pt/Fe₂O₃ with Pt–Fe pair sites as a catalyst for oxygen reduction with ultralow Pt loading, *Nat. Energy* 6 (2021) 614–623, <https://doi.org/10.1038/s41560-021-00826-5>.
- [26] S. Zhao, Z. Ma, Z. Wan, J. Li, X. Wang, Noble-metal-free FeMn–N–C catalyst for efficient oxygen reduction reaction in both alkaline and acidic media, *J. Colloid Interface Sci.* 642 (2023) 800–809, <https://doi.org/10.1016/j.jcis.2023.03.206>.
- [27] Y. Zheng, A.S. Petersen, H. Wan, R. Hübner, J. Zhang, J. Wang, H. Qi, Y. Ye, C. Liang, J. Yang, Z. Cui, Y. Meng, Z. Zheng, J. Rossmeisl, W. Liu, Scalable and Controllable synthesis of Pt–Ni bunched-nanocages aerogels as efficient electrocatalysts for oxygen reduction reaction, *Adv. Energy Mater.* 13 (2023) 2204257, <https://doi.org/10.1002/aenm.202204257>.
- [28] T. Ali, H. Wang, W. Iqbal, T. Bashir, R. Shah, Y. Hu, Electro-synthesis of organic compounds with heterogeneous catalysis, *Adv. Sci.* 10 (2023) 2205077, <https://doi.org/10.1002/adv.202205077>.
- [29] H. Cai, G. Zhang, X. Zhang, B. Chen, Z. Lu, H. Xu, R. Gao, C. Shi, Engineering the local coordination environment and density of FeN₄ sites by Mn cooperation for electrocatalytic oxygen reduction, *Small* 18 (2022) 2200911, <https://doi.org/10.1002/sml.202200911>.
- [30] H. Liu, L. Jiang, J. Khan, X. Wang, J. Xiao, H. Zhang, H. Xie, L. Li, S. Wang, L. Han, Decorating single-atomic Mn sites with FeMn clusters to boost oxygen reduction reaction, *Angew. Chem. Int. Ed.* 62 (2023), <https://doi.org/10.1002/anie.202214988>.
- [31] S. Zhao, J. Li, R. Wang, J. Cai, S. Zhang, Electronically and geometrically modified single-atom Fe sites by adjacent Fe nanoparticles for enhanced oxygen reduction, *Adv. Mater.* 34 (2022) 2107291, <https://doi.org/10.1002/adma.202107291>.
- [32] X. Han, X. Ling, Y. Wang, T. Ma, C. Zhong, W. Hu, Y. Deng, Generation of nanoparticle, atomic-cluster, and single-atom cobalt catalysts from zeolitic imidazole frameworks by spatial isolation and their use in zinc–air batteries, *Angew. Chem. Int. Ed.* 58 (2019) 5359–5364, <https://doi.org/10.1002/anie.201901109>.
- [33] T. Lu, H. Wang, Graphdiyne-supported metal electrocatalysts: from nanoparticles and cluster to single atoms, *Nano Res.* 15 (2022) 9764–9778, <https://doi.org/10.1007/s12274-022-4157-1>.
- [34] X. Wan, Q. Liu, J. Liu, S. Liu, X. Liu, L. Zheng, J. Shang, R. Yu, J. Shui, Iron atom–cluster interactions increase activity and improve durability in Fe–N–C fuel cells, *Nat. Commun.* 13 (2022) 2963, <https://doi.org/10.1038/s41467-022-30702-z>.
- [35] H. Shang, Z. Jiang, D. Zhou, J. Pei, Y. Wang, J. Dong, X. Zheng, J. Zhang, W. Chen, Engineering a metal–organic framework derived Mn–N₄–C₂S₂ atomic interface for highly efficient oxygen reduction reaction, *Chem. Sci.* 11 (2020) 5994–5999, <https://doi.org/10.1039/D0SC02343D>.
- [36] H. Shang, W. Sun, R. Sui, J. Pei, L. Zheng, J. Dong, Z. Jiang, D. Zhou, Z. Zhuang, W. Chen, J. Zhang, D. Wang, Y. Li, Engineering isolated Mn–N₂C₂ atomic interface sites for efficient bifunctional oxygen reduction and evolution reaction, *Nano Lett.* 20 (2020) 5443–5450, <https://doi.org/10.1021/acs.nanolett.0c01925>.
- [37] L. Gong, J. Zhu, F. Xia, Y. Zhang, W. Shi, L. Chen, J. Yu, J. Wu, S. Mu, Marriage of ultralow platinum and single-atom MnN₄ moiety for augmented ORR and HER catalysis, *ACS Catal.* 13 (2023) 4012–4020, <https://doi.org/10.1021/acscatal.2c06340>.
- [38] Y. Deng, J. Pang, W. Ge, M. Zhang, W. Zhang, W. Zhang, M. Xiang, Q. Zhou, J. Bai, Constructing atomically-dispersed Mn on ZIF-derived nitrogen-doped carbon for boosting oxygen reduction, *Front. Chem.* 10 (2022) 969905, <https://doi.org/10.3389/fchem.2022.969905>.
- [39] Y. Lian, W. Yang, C. Zhang, H. Sun, Z. Deng, W. Xu, L. Song, Z. Ouyang, Z. Wang, J. Guo, Y. Peng, Unpaired 3d electrons on atomically dispersed cobalt centres in coordination polymers regulate both oxygen reduction reaction (ORR) activity and selectivity for use in zinc–air batteries, *Angew. Chem. Int. Ed.* 59 (2020) 286–294, <https://doi.org/10.1002/anie.201910879>.
- [40] Y. Dai, B. Liu, Z. Zhang, P. Guo, C. Liu, Y. Zhang, L. Zhao, Z. Wang, Tailoring the d-orbital splitting manner of single atomic sites for enhanced oxygen reduction, *Adv. Mater.* 35 (2023) 2210757, <https://doi.org/10.1002/adma.202210757>.
- [41] T. Cui, Y. Wang, T. Ye, J. Wu, Z. Chen, J. Li, Y. Lei, D. Wang, Y. Li, Engineering dual single-atom sites on 2D ultrathin N-doped carbon nanosheets attaining ultra-low-temperature Zinc–Air battery, *Angew. Chem. Int. Ed.* 61 (2022), <https://doi.org/10.1002/anie.202115219>.
- [42] X. Ao, W. Zhang, Z. Li, J.-G. Li, L. Soule, X. Huang, W.-H. Chiang, H.M. Chen, C. Wang, M. Liu, X.C. Zeng, Markedly enhanced oxygen reduction activity of single-atom Fe catalysts via integration with Fe nanoclusters, *ACS Nano* 13 (2019) 11853–11862, <https://doi.org/10.1021/acsnano.9b05913>.
- [43] Y. Xie, X. Chen, K. Sun, J. Zhang, W. Lai, H. Liu, G. Wang, Direct oxygen–oxygen cleavage through optimizing interatomic distances in dual single-atom electrocatalysts for efficient oxygen reduction reaction, *Angew. Chem. Int. Ed.* 62 (2023) e202301833, <https://doi.org/10.1002/anie.202301833>.
- [44] B. Ji, J. Gou, Y. Zheng, X. Pu, Y. Wang, P. Kidkhunthod, Y. Tang, Coordination chemistry of large-sized yttrium single-atom catalysts for oxygen reduction reaction, *Adv. Mater.* (2023) 2300381, <https://doi.org/10.1002/adma.202300381>.
- [45] S. Wu, S. Jiang, S.-Q. Liu, X. Tan, N. Chen, J.-L. Luo, S.H. Mushrif, K. Cadien, Z. Li, Single Cu–N 4 sites enable atomic Fe clusters with high-performance oxygen reduction reactions, *Energy Environ. Sci.* 16 (2023) 3576–3586, <https://doi.org/10.1039/D3EE00840A>.
- [46] P. Li, F. Qiang, X. Tan, Z. Li, J. Shi, S. Liu, M. Huang, J. Chen, W. Tian, J. Wu, W. Hu, H. Wang, Electronic modulation induced by decorating single-atomic Fe–Co pairs with Fe–Co alloy clusters toward enhanced ORR/OER activity, *Appl. Catal. B: Environ.* 340 (2024) 123231, <https://doi.org/10.1016/j.apcatb.2023.123231>.
- [47] H. Wang, W. Wang, H. Yu, Q. Mao, Y. Xu, X. Li, Z. Wang, L. Wang, Interface engineering of polyaniline-functionalized porous Pd metallene for alkaline oxygen reduction reaction, *Appl. Catal. B: Environ.* 307 (2022) 121172, <https://doi.org/10.1016/j.apcatb.2022.121172>.
- [48] S. Ji, T. Liu, L. Leng, H. Liu, J. Zhang, M. Zhang, Q. Xu, J. Zhu, M. Qiao, Y. Wang, J. H. Horton, Z. Li, Protein-mediated synthesis of iron single atom electrocatalyst with highly accessible active sites for enhanced pH-universal oxygen reduction, *Appl. Catal. B: Environ.* 320 (2023) 121987, <https://doi.org/10.1016/j.apcatb.2022.121987>.
- [49] C. Qi, H. Yang, Z. Sun, H. Wang, N. Xu, G. Zhu, L. Wang, W. Jiang, X. Yu, X. Li, Q. Xiao, P. Qiu, W. Luo, Modulating electronic structures of iron clusters through orbital rehybridization by adjacent single copper sites for efficient oxygen reduction, *Angew. Chem. Int. Ed.* 62 (2023) e202308344, <https://doi.org/10.1002/anie.202308344>.
- [50] K. Wang, H. Yang, Q. Wang, J. Yu, Y. He, Y. Wang, S. Song, Y. Wang, Electronic enhancement engineering by atomic Fe–N₄ sites for highly-efficient PEMFCs: tailored electric-thermal field on Pt surface, *Adv. Energy Mater.* 13 (2023) 2204371, <https://doi.org/10.1002/aenm.202204371>.
- [51] L. Yan, Z. Xu, X. Liu, S. Mahmood, J. Shen, J. Ning, S. Li, Y. Zhong, Y. Hu, Integrating trifunctional Co@NC–CNTs@NiFe–LDH electrocatalysts with arrays of porous triangle carbon plates for high-power-density rechargeable Zn–air batteries

- and self-powered water splitting, *Chem. Eng. J.* 446 (2022) 137049, <https://doi.org/10.1016/j.cej.2022.137049>.
- [52] L. Yan, B. Xie, C. Yang, Y. Wang, J. Ning, Y. Zhong, Y. Hu, Engineering self-supported hydrophobic-aerophilic air cathode with CoS/Fe₃S₄ nanoparticles embedded in S, N Co-doped carbon plate arrays for long-life rechargeable Zn-Air batteries, *Adv. Energy Mater.* 13 (2023) 2204245, <https://doi.org/10.1002/aenm.202204245>.
- [53] S. Wang, H. Wang, C. Huang, P. Ye, X. Luo, J. Ning, Y. Zhong, Y. Hu, Trifunctional electrocatalyst of N-doped graphitic carbon nanosheets encapsulated with CoFe alloy nanocrystals: the key roles of bimetal components and high-content graphitic-N, *Appl. Catal. B: Environ.* 298 (2021) 120512, <https://doi.org/10.1016/j.apcatb.2021.120512>.